Effect of moisture condensation on the morphology and intensity of idealized thermoconvective vertical vortices

J. Cortés [1], D. Castaño[2], M. R. Turner[3] and M. C. Navarro*[4]

[1] Departamento de Matemáticas, Escuela Técnica Superior de Ingeniería Industrial de Ciudad Real-IMACI
Universidad de Castilla-La Mancha, 13071 Ciudad Real, Spain.

[2] Departamento de Matemáticas, Escuela de Ingeniería Industrial y Aeroespacial-IMACI
Universidad de Castilla-La Mancha, 45071 Toledo, Spain.

[3] School of Mathematics and Physics, University of Surrey, Guildford, GU2 7XH. United Kingdom.

[4] Departamento de Matemáticas, Facultad de Ciencias y Tecnologías Químicas-IMACI
Universidad de Castilla-La Mancha, 13071 Ciudad Real, Spain.

* Corresponding author: María Cruz Navarro, Departamento de Matemáticas, Facultad de Ciencias y Tecnologías Químicas, Universidad de Castilla-La Mancha, Avda. Camilo José Cela 10, 13071 Ciudad Real, Spain. e-mail: MariaCruz.Navarro@uclm.es

Abstract

In this study we investigate the effects of moisture condensation on the structure and intensity of bottom-up and top-down generated thermoconvective vortices, which develop in a rotating cylindrical domain with localized thermal gradients imposed at the upper and lower boundaries. Numerical simulations are performed using an idealized moist-convection model that incorporates latent heat release through a fast-condensation approximation. The results show that condensation substantially modifies the transition from a single-cell to a two-cell vortex, a transition that is known to occur in dry-air vortices as thermal and rotational parameters are varied. For bottom-up vortices, latent heat release occurs primarily in the upper part of the vortex, promoting stronger buoyancy-driven circulation and leading to a substantial increase in vortex intensity. A detailed force-balance analysis reveals the mechanisms responsible for this enhancement. In contrast, for top-down vortices, condensation primarily alters the vortex morphology and generally weakens its rotational intensity. These findings highlight the different roles played by condensation in the two vortex configurations and contribute to a better understanding of moist thermoconvective vortex dynamics.

1 Introduction

The importance of thermal gradients in the formation, evolution, and intensification of all types of atmospheric vortices is well established [1–6]. Observational studies of dust devils have revealed the presence of strong horizontal and vertical temperature gradients within these structures [1]. Likewise, the scaling theory proposed by [7], and subsequently validated against field observations [8],

predicts that dust-devil intensity depends on the product of two thermodynamic efficiencies corresponding to horizontal and vertical thermal gradients. Temperature contrasts between different air masses are a key ingredient in the formation of mesocyclones and the subsequent development of tornadoes [3].

This paper focuses on developed thermoconvective vertical vortices in small scale, idealised scenarios. Previous numerical studies of dry-air vortices [9–11] have demonstrated that thermal gradients strongly influence their formation, morphology, evolution, and intensity. In particular, [9] also examined the role of ambient rotation and showed that it is a crucial parameter governing the structure and stability of these vortices. The objective of the present study is to extend these investigations to moist-air conditions and determine how condensation modifies the morphology, dynamics, and intensity of thermoconvective vertical vortices. While our ultimate aim is to investigate large scale systems, such as those in the atmosphere, this preliminary, proof of concept study is far from this scenario as we wish to only consider low Rayleigh number scenarios where the flow can be considered as laminar. However, these results illuminate important information on how the morphology of these structures behave when moisture is present.

The condensation of water vapor in air into liquid water, which then *rains out* of a physical system, is an important physical feature, such as in the Earth's atmosphere. On large scales, this process is responsible for large vertical atmospheric fluxes of entropy, mass and momentum, particularly in tropical regions, and is often studied using idealized one-dimensional column models designed to isolate the thermodynamic processes associated with moist convection (see [12–15] and references therein). Accurately representing condensation processes is also essential for climate modeling. Since convection occurs at small scales that strongly influences large-scale phenomena such as the Hadley circulation, it remains a key source of uncertainty in climate models and hence its study in any context is useful [16, 17].

The dynamical importance of condensation stems from the strong coupling between moisture and buoyancy. As moist air rises and cools, the amount of water vapour that can be sustained in equilibrium decreases according to the Clausius–Clapeyron relation. Once saturation is reached, condensation occurs and latent heat is released into the surrounding air. This release of thermal energy enhances buoyancy, thereby strengthening the vertical motion that generated the conden-

sation in the first place. Because the latent heat of condensation is large, even relatively small amounts of condensed water can produce substantial heating and significantly alter the flow dynamics. In our small scale, idealised problem we also expect this additional heating to be significant, driving phenomenological differences to the dry-air vortex case, and this study aims to identify those differences.

To incorporate the effects of condensation into our vortex model, we adopt the idealized moist-convection framework introduced by [22, 23], which extends the classical Rayleigh–Bénard problem to include moisture and latent heat release. In this model, a source of water vapour is provided through prescribed moist boundary conditions, allowing moisture to be continuously supplied to the system. The flow is driven by an imposed temperature difference between the upper and lower boundaries. As warm, moist air rises, it cools as it mixes with the surrounding colder air. If the air cools sufficiently to reach saturation, as determined by the Clausius–Clapeyron relation, condensation occurs. At this point, excess moisture is instantaneously removed from the system, thereby excluding a mixed liquid-water phase and supersaturation, and converted into thermal energy through latent heat release, which enhances buoyancy and further strengthens the convective motion.

A major advantage of this formulation is that it retains the essential physical mechanism of latent heat release while remaining sufficiently simple for detailed mathematical and numerical analysis. Consequently, it has become an attractive framework for investigating the fundamental dynamics of moist convection. Oishi & Brown [24] and Dritschel *et al.* [17] performed linear stability analyses of the model proposed by Vallis *et al.* [22, 23], using slightly different boundary conditions, to identify the principal instability mechanisms governing moist convection. More recently, Agasthya *et al.* [25] carried out nonlinear simulations of the same model to derive scaling relationships as used in cloud-resolving models.

Building on these developments, we employ this idealized moist-convection framework to investigate the mathematical modeling and numerical simulation of thermoconvective vortices in moist air. Our primary objective is to determine how condensation affects both the morphology and the intensity of the vortices, and how these effects depend on the thermal forcing imposed at the upper and lower boundaries as well as on the ambient rotation rate. Simplified convection models

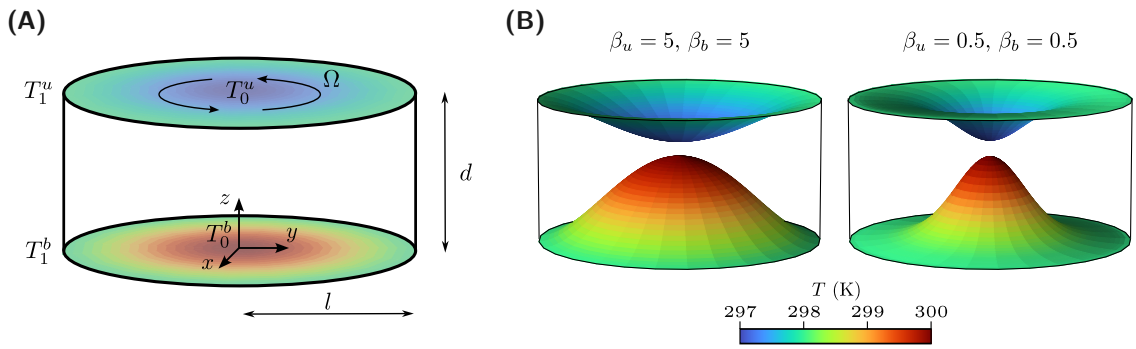

Figure 1: Illustration of the physical domain and thermal boundary conditions. (A) Sketch of the cylindrical domain showing representative temperature contours on the top and bottom boundaries. (B) Influence of the parameter β on the sharpness of the boundary temperature distributions. The surfaces represent the temperature distributions on the top and bottom boundaries of the cylinder. Left, $\beta_u = \beta_b = 5$, right, $\beta_u = \beta_b = 0.5$. In both panels, $T_1^u = T_1^b = 298$ K, $T_0^u = 297$ K, and $T_0^b = 300$ K.

have proved valuable in a wide range of atmospheric applications because they enable the isolation of key physical mechanisms without the need to resolve the multitude of small-scale processes present in the real atmosphere [26–28]. Likewise, the moist Rayleigh–Bénard framework introduced in [22] provides an ideal setting for investigating how condensation influences the structure and dynamics of thermoconvective vortices.

The paper is organized as follows. Section 2 introduces the mathematical model and describes the numerical scheme used to simulate it. The numerical results are presented and discussed in Section 3. Finally, the main conclusions and directions for future work are summarized in Section 4.

2 Formulation

2.1 Mathematical model

The model used in this work is rotating Rayleigh-Bénard convection, which has been widely applied for studying the fundamental processes underlying phenomena such as tornadoes, dust devils and mesocyclones [6, 9–11, 29]. The effect of condensation of moist air is added into this model using the idealised condensation model proposed in [22, 23].

The model domain is a rotating cylindrical container of dimensions l meters (radius) and

d meters (height), with Ω being the rotation rate of the domain, which is not related to the rotation rate of the Earth, but instead models the rotation rate of parent weather systems for example [29]. In the following, (r, φ, z) denotes the usual cylindrical polar coordinates with the z-axis oriented in the axial direction. The rotation rate range is chosen so that stationary axisymmetric vortices are found for a wide range of temperature differences in the dry case [10]. See Figure 1(A) for a schematic of the flow domain. Horizontal temperature differences are set at both the upper and lower boundaries. At the upper surface, a cold drop is considered localized at the central part. To establish this, a Gaussian profile for temperature is considered, which takes the minimum value T_0^u at $r = 0$ and the maximum value T_1^u at $r = l$. We define $\Delta T_r^u = T_0^u - T_1^u$. The precise form of the temperature distribution at the upper surface is

$$T_u(r) = A_u \exp\left[\left(\frac{1}{\beta_u} - \frac{r^2}{l^2\beta_u}\right)^2\right] + \epsilon_u, \tag{1}$$

where $A_u = \Delta T_r^u / \left[\exp(1/\beta_u^2) - 1\right]$, $\epsilon_u = T_1^u - A_u$, and β_u is a parameter that measures the sharpness of the Gaussian profile. Smaller values of β_u correspond to localized cooling on the top, while larger values of β_u define a more spread cooling at $z = d$ (see Figure 1(B)).

At the lower surface, a heat source is established at the center. Again, a Gaussian profile for temperature is considered, which takes the value $T_0^b \geq T_0^u$ at $r = 0$ and the value T_1^b at $r = l$. We define $\Delta T_r^b = T_0^b - T_1^b$, which denotes the horizontal temperature difference at the bottom. The distribution of temperature at the bottom surface is

$$T_b(r) = A_b \exp\left[\left(\frac{1}{\beta_b} - \frac{r^2}{l^2\beta_b}\right)^2\right] + \epsilon_b \tag{2}$$

where $A_b = \Delta T_r^b / \left[\exp(1/{\beta_b}^2) - 1\right]$, $\epsilon_b = T_1^b - A_b$, and again β_b models the sharpness of the thermal profile. Smaller values of β_b correspond to localized heating on the bottom, while larger values of β_b define a more spread heating at $z = 0$ (see Figure 1(B)). Additionally, we define the vertical temperature difference, $\Delta T_v = T_0^b - T_0^u > 0$, and the dimensionless parameters $\delta^u = \Delta T_r^u / \Delta T_v$, and $\delta^b = \Delta T_r^b / \Delta T_v$. When $|\delta^u| > \delta^b$ the vortex develops top-down, when $|\delta^u| < \delta^b$ the vortex develops from the bottom-up [11]. In the numerical simulations in this paper, we keep fixed $T_1^u = T_1^b = 298$ K and $\delta^u = -1/3$ and $\delta^b = 2/3$ for the case of bottom-up vortices, and $\delta^u = -2/3$ and $\delta^b = 1/3$ for the case of top-down vortices. Figure 1(B) shows the influence of the parameters β_b and β_u on the sharpness of the boundary temperature distributions.

We assume that the effect of compressibility is small for the vortices we consider, which is consistent with the works of [30, 31], hence the air can be modeled as an incompressible fluid. The equations governing the system, considering the Oberbeck-Boussinesq approximation, are the Navier-Stokes equations (continuity equation and momentum equations),

$$\nabla \cdot \boldsymbol{u} = 0, \tag{3}$$

$$\rho_0 \partial_t \boldsymbol{u} + \rho_0 \left(\boldsymbol{u} \cdot \nabla\right) \boldsymbol{u} = -\nabla p + \mu \nabla^2 \boldsymbol{u} - \rho_0 (1 - \alpha(T - T_0)) g \mathbf{e}_z - 2\rho_0 \Omega \mathbf{e}_z \times \boldsymbol{u}; \tag{4}$$

the heat equation,

$$\rho_0 C_p \partial_t T + \rho_0 C_p \boldsymbol{u} \cdot \nabla T = \kappa \nabla^2 T + Q, \tag{5}$$

where $Q = L M_v \frac{(c_v - c_{sat}}{)} \tau \mathcal{H}(c_v - c_{sat})$ represents the heat source from the condensation process; and the equation for the transport of water vapor concentration,

$$\partial_t c_v + \boldsymbol{u} \cdot \nabla c_v = D \nabla^2 c_v + G, \tag{6}$$

where $G = -\frac{(c_v - c_{sat}}{)} \tau \mathcal{H}(c_v - c_{sat})$ represents the contribution from the condensation process. In Equations (3)-(6), $\boldsymbol{u}$ is the velocity field, p the pressure, T the absolute temperature, c_v the vapor concentration, c_{sat} the vapor saturation concentration, t time, and $\mathbf{e}_z$ is a unit vector in the z-direction. The function $\mathcal{H}(\cdot)$ is the Heaviside function and implies that condensation only occurs when $c_v > c_{sat}$, i.e. if the vapor concentration is above the saturated concentration level. We do not allow for supersaturation in this problem, i.e., $c_v > c_{sat}$ for more than one time-step, hence if after a time-step of the integration scheme $c_v > c_{sat}$, then condensation occurs at those grid points and latent heat is added to the system.

Within the Oberbeck–Boussinesq approximation, buoyancy is assumed to depend exclusively on temperature-induced density variations. The contribution of water-vapor concentration to density changes (virtual-temperature effect) is neglected, so that moisture affects the dynamics only through condensation and the associated latent-heat release. This approximation is adopted to isolate the dynamical role of latent heating and to maintain a minimal model formulation. Note that in the system (3)-(5) the effect of adiabatic expansion is not included, as the results presented in this work are for a small domain ($d = 2$ cm), and so it is assumed the adiabatic expansion effect would be negligible. However, if the model were to be extended to large-scale atmospheric systems,

such as tornadoes, then this effect would need to be incorporated, for example by using potential temperature or buoyancy rather than the physical temperature.

The vapor saturation concentration model is given by

$$c_{sat} = \frac{p_{sat}}{p_v} c_v, \tag{7}$$

where p_{sat} is the saturation pressure of water vapor [32],

$$p_{sat}(T) = 610.7 \times 10^{7.5\frac{T-273.15}{T-35.85}}, \tag{8}$$

and p_v is the water vapor partial pressure, $p_v = p - p_a$, where p_a is the dry air partial pressure. Equations (7)-(8) together make up the Clausius-Clapeyron relation, which allows computing c_{sat}, the vapor concentration at which fluid parcels become saturated, as a function of T and p. The values of the coefficients in (8) are determined for the Earth, and are valid for $233\,\mathrm{K} \leq T \leq 313\,\mathrm{K}$. Additionally, the values of p_{sat} agree with those in the Smithsonian Meteorological Tables to within 0.2%. The physical parameters in the governing equations are: α the coefficient of volume thermal expansion, ρ_0 the density of air, g the gravity constant, μ the dynamic viscosity of the fluid, C_p the fluid heat capacity at constant pressure, κ the fluid thermal conductivity, L the latent heat for condensation, M_v the molar mass of water vapor, τ the time scale for condensation and D the vapor diffusion coefficient in air. The vapor diffusivity D is used as an effective transport coefficient. Since the model is formulated in a computational domain whose dimensions are much smaller than those of real atmospheric vortices, using the atmospheric molecular diffusivity would increase the relative importance of diffusive transport at the model scale and would lead to excessive smoothing of moisture gradients. The lower value of D was chosen to preserve advection-dominated moisture transport. The material properties ρ_0, μ, α, C_p and κ are evaluated at the reference pressure, $p_0 = 1$ atm, and temperature, $T_0 = (T_1^u + T_1^b)/2$. The values of the parameters used in computations are summarized in Table 1.

The time scale for condensation, τ, is chosen to be smaller than any other dynamical timescale in our system, such that we are in the 'fast condensation limit'. In this limit we assume that all the condensate is removed from the system immediately so that no liquid water is present. This is a simplification to the actual condensation process and avoids complications of processes which occur when multiple water states are present [33, 34].

The boundary conditions used at the edge of the computational domain for the velocity field are slip boundary conditions

$$\boldsymbol{u} \cdot \boldsymbol{n} = 0, \qquad \boldsymbol{K}_n - (\boldsymbol{K}_n \cdot \boldsymbol{n})\, \boldsymbol{n} = \boldsymbol{0}, \tag{9a}$$

$$\boldsymbol{K}_n = \mu \left[\nabla \boldsymbol{u} + (\nabla \boldsymbol{u})^{\top}\right] \cdot \boldsymbol{n}, \tag{9b}$$

where $\boldsymbol{n}$ denotes the outward normal vector to the surface, and $\boldsymbol{K}_n$ is the viscous stress vector acting on the surface whose unit normal is $\boldsymbol{n}$. For the temperature field, at the lateral wall $r = l$, an insulating boundary condition is imposed

$$\boldsymbol{n} \cdot \nabla T = \boldsymbol{0}, \tag{10}$$

while at the top, $z = d$, and at the bottom, $z = 0$, the non-uniform temperature distributions $T_u(r)$ and $T_b(r)$, defined in Equations (1) and (2), are used.

Additionally, at the top and bottom boundaries the concentration of vapor is considered at its saturated value

$$c_v(z = d) = c_{sat}(T_u(r)), \tag{11}$$

$$c_v(z = 0) = c_{sat}(T_b(r)), \tag{12}$$

while at the lateral wall ($r = l$) we consider an insulation condition for the vapor concentration, which means there is no moisture flux across the boundary,

$$\boldsymbol{n} \cdot \nabla c_v = \boldsymbol{0}. \tag{13}$$

The initial conditions for the time-marching scheme are $\boldsymbol{u} = \boldsymbol{0}$, $p = p_0$, $T = T_0$ and $c_v = c_{sat}(T_0)$. For numerical convenience, both the imposed temperature differences, ΔT_r^u and ΔT_r^b, and the rotation rate, Ω, are gradually ramped from zero to their target values during an initial time interval. This procedure mitigates inconsistencies between the boundary conditions and the governing equations at the onset of the simulation.

The simulation is then integrated forward in time until a steady state is achieved.

2.2 Numerical Implementation

Numerical simulations of the system of equations in Section 2.1 have been performed using the software COMSOL Multiphysics® v6.1 [35]. The following packages have been used:

Description	Parameter	Value
Radius of the cylinder	l (m)	0.0335
Height of the cylinder	d (m)	0.02
Rotation rate	Ω (s^{-1})	0.1 – 0.6
Sharpness of the heat profile at the bottom	β_b	0.5 – 5
Sharpness of the cold profile at the top	β_u	0.5 – 5
Coefficient of volume expansion	α (K^{-1})	3.44×10^{-3}
Temperature at outer part of the top	T_1^u (K)	298
Temperature at inner part of the top	T_0^u (K)	291.33 – 297.67
Temperature at outer part of the bottom	T_1^b (K)	298
Temperature at inner part of the bottom	T_0^b (K)	298.33 – 304.67
Density at T_0	ρ_0 ($kg\,m^{-3}$)	1.2
Dynamic viscosity	μ (N s m^{-2})	1.8×10^{-5}
Heat capacity at constant pressure	C_p ($kJ\,molK^{-1}$)	0.029
Thermal conductivity	κ (W $m^{-1}\,K^{-1}$)	0.026
Latent heat for condensation	L ($kJ\,kg^{-1}$)	2500
Molar mass of water vapor	M_v ($kg\,mol^{-1}$)	0.018
Vapor diffusion coefficient in air	D ($m^2\,s^{-1}$)	1×10^{-6}
Dry air partial pressure	p_a (Pa)	101325
Time scale for condensation	τ (s)	0.5

Table 1: Parameters considered for the experiment.

1. *Laminar flow:* The Laminar Flow package is used to calculate the velocity and pressure fields of the fluid. The package is set up to solve the incompressible Navier-Stokes equations (3)-(4) with slip boundary conditions. Gravity and Coriolis forces are added as body forces, and the fluid properties are those for air (see Table 1).

2. *Heat transfer in liquids:* In the problem there is heat transfer by convection in the fluid. This package couples the heat equation (5) to the Navier-Stokes equations.

3. *Moisture transport in air:* The Moisture Transport in Air package is used to model moisture transport through convection and diffusion of vapor in moist air via (6).

To introduce the Heaviside function $\mathcal{H}(c_v - c_{sat})$ in the simulated model, we have used the COMSOL function flc2hs, a smoothed Heaviside function with a continuous second derivative without

overshoot. The definition of flc2hs is

$$\begin{aligned}
&\text{flc2hs}(c_v - c_{sat}, s) = 0, \qquad \text{if} \qquad c_v - c_{sat} \leq -s \\
&\text{flc2hs}(c_v - c_{sat}, s) = 1, \qquad \text{if} \qquad c_v - c_{sat} \geq s \\
&\text{flc2hs}(c_v - c_{sat}, s) = 0.5 + 0.9375 \left(\frac{c_v - c_{sat}}{s} \right) - 0.625 \left(\frac{c_v - c_{sat}}{s} \right)^3 + 0.1875 \left(\frac{c_v - c_{sat}}{s} \right)^5 \\
&\qquad\qquad\qquad\qquad\qquad\qquad\qquad\qquad\qquad\qquad \text{if} \qquad -s < c_v - c_{sat} < s
\end{aligned}$$

where s is the scale value defining the smoothing zone. We have set $s = 10^{-6}$ in our computations, but we find other similar values give almost identical results.

COMSOL Multiphysics® applies the finite element method to spatially discretize the governing partial differential equations. In this work, the laminar flow is discretized using $P1 + P1$ elements, that is, both velocity and pressure are interpolated using piecewise linear polynomials. For temperature and vapor concentration a linear spatial discretization is used as well. Similarly to [36], a stabilized finite element formulation featuring streamline diffusion and crosswind diffusion is employed. The time-marching scheme is based on a backward differentiation formula (BDF) solver with variable order and automatic step-size control. The maximum order is restricted to two. Since the BDF solver is implicit, each time step requires the solution of a nonlinear system. This nonlinear problem is solved using a damped Newton method with a constant damping factor of 0.7, updating the Jacobian once per time step. Finally, the linear systems produced by the Newton method are handled by the multifrontal massively parallel sparse direct solver (MUMPS).

A convergence study of the numerical scheme undertaken by increasing the number of elements in the mesh is provided in the Appendix A.

3 Results

In this section, the dry and moist air scenarios are analysed and compared in the bottom-up and top-down forming vortex configurations. Throughout the manuscript, the term "dry" refers to simulations with $L = 0$, for which condensation does not affect the dynamics, whereas the term "moist" refers to simulations with active condensation and latent-heat release.

Within the range of parameters considered for computations (Table 1), the Rossby number is of order $Ro = O(1)$, indicating that inertial and rotational effects are of comparable magnitude.

This supports our statement that the imposed rotation rate is not intended to represent the Earth's rotation but the rotation of the parent system in which the vortex develops.

The Reynolds number is of order $Re = O(10) - O(10^2)$ and the Rayleigh number of order $Ra = O(10^2) - O(10^3)$. These values confirm that the present simulations operate in a laminar rotating-convection regime. These values are several orders of magnitude smaller than those typically encountered in atmospheric flows. Our intention is not to perform a quantitative comparison with atmospheric vortices but design an idealized small-scale framework aimed at isolating the dynamical role of condensation.

3.1 Case 1: bottom-up vortices

We first consider the case $\delta^u = -1/3$ and $\delta^b = 2/3$, corresponding to a bottom-up forming vortex, with $\beta_u = 5$. A series of numerical simulations were conducted by varying the thermal parameters, ΔT_v and β_b, and the ambient rotation rate Ω.

3.1.1 Transition from a one-cell vortex to a two-celled vortex

To set a control scenario, we begin with simulations of the dry-air case. The first steady-state solution obtained corresponds to a well-developed vertical single-cell vortex that extends from the bottom of the domain to top. Figure 2(A) shows three-dimensional isosurfaces of the vertical vorticity,

$$\omega_z = \frac{1}{r}\left(\frac{\partial}{\partial r}(r u_\varphi) - \frac{\partial u_r}{\partial \varphi}\right),$$

for several contour levels. Figures 2(B)-(E) present contours of temperature and the three velocity components on the plane $y = 0$. Note that u_r and u_φ denote the radial and azimuthal components of the velocity field $\boldsymbol{u}$. The horizontal temperature gradient imposed at the lower boundary generates an inward radial flow toward the center of the cylinder. Upon reaching the central region, the fluid ascends along the cylinder axis while simultaneously increasing its azimuthal velocity. Near the top of the domain, the flow turns radially outward toward the lateral boundary and subsequently descends, forming a recirculation cell. For the parameter values considered, the resulting vortex is stationary and axisymmetric within the cylindrical domain.

The value of ΔT_v strongly influences the vortex structure. As ΔT_v increases, a column of descending cooler air emerges along the central axis of the vortex, creating a central region with

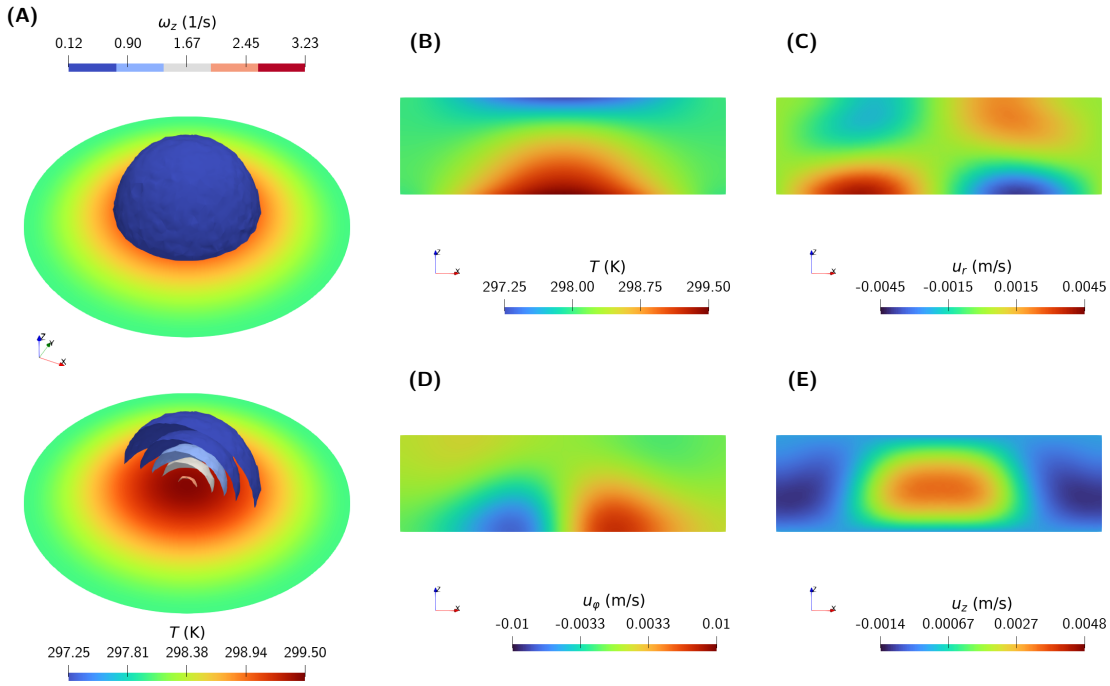

Figure 2: One-cell stationary vortex for the dry case obtained for $\beta_b = 5$, $\Delta T_v = 2.25$ K, $\Omega = 0.4$ rad/s, and $L = 0$ J/kg. Panel (A) shows isosurfaces of the vertical vorticity, ω_z, together with a slice at $z = 0.01d$ of the temperature field. Panels (B)-(E) show slices at $y = 0$ of the temperature field and the radial, azimuthal, and vertical components of the velocity field, respectively. In panels (B)-(E), the OY axis points inward.

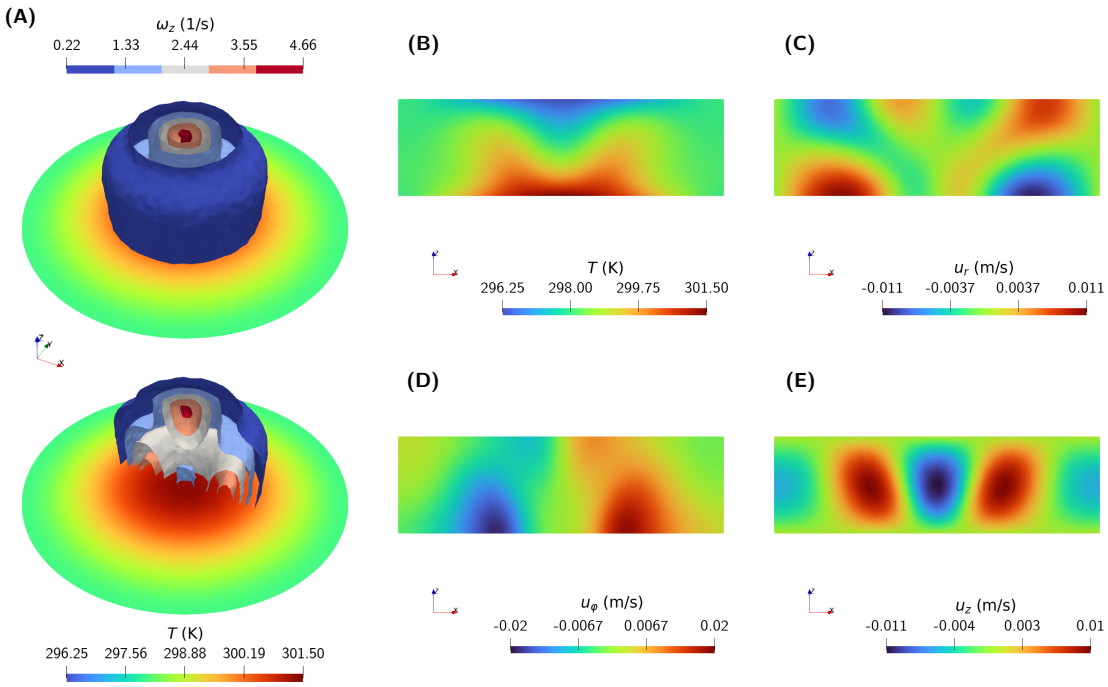

Figure 3: Two-celled stationary vortex for the dry case obtained for $\beta_b = 5$, $\Delta T_v = 5.25$ K, $\Omega = 0.4$ rad/s, and $L = 0$ J/kg. Panel (A) shows isosurfaces of the vertical vorticity, ω_z, together with a slice at $z = 0.01d$ of the temperature field. Panels (B)-(E) show slices at $y = 0$ of the temperature field and the radial, azimuthal, and vertical components of the velocity field, respectively. In panels (B)-(E), the OY axis points inward.

substantially reduced rotation. Figure 3 illustrates the formation of this central downdraft through the vertical velocity field, u_z. The progressive radial expansion of the descending region is clearly visible in the vertical velocity profiles, as well as in the temperature field, where a tongue of cooler air (blue) penetrates into the region occupied by warmer air (red). As a result, the initially single-cell vortex transitions into a *two-cell vortex*, characterized by a central downdraft surrounded by two regions of ascending warm air. The onset of this transition occurs at $\Delta T_v = 3.25\,\mathrm{K}$, while the two-cell structure becomes fully established by $\Delta T_v = 5\,\mathrm{K}$.

A radial force balance reveals the physical mechanism responsible for the formation of the two-cell vortex. Four terms appear in the radial momentum equation: the inertial force, $(\rho_0(\boldsymbol{u}\cdot\nabla)\boldsymbol{u})_r$; the pressure-gradient force, $\partial_r p$; the viscous force, $(\nu\nabla^2\boldsymbol{u})_r$; and the Coriolis force, $(2\rho_0\Omega\boldsymbol{e}_z\times\boldsymbol{u})_r$, where the subscript r denotes the radial component. In comparison with pressure-

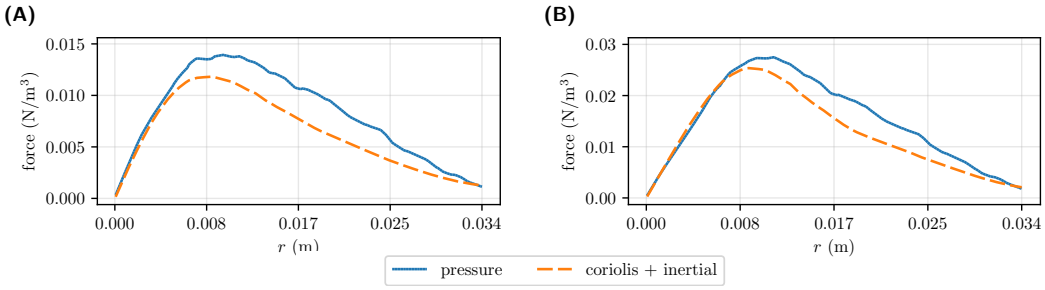

Figure 4: Radial profile at $z = 0.1d$ of the radial pressure gradient and the radial component of the sum of the inertial and the Coriolis force. Panel (A) corresponds to $\Delta T_v = 2.25$ K, for which the stationary solution is a single-cell vortex. Panel (B) corresponds to $\Delta T_v = 3.5$ K, for which the stationary solution begins to develop the characteristic central downdraft of double-cell vortices.

gradient, rotational and inertial contributions, the viscous term acts mainly as a dissipative mechanism and does not govern the qualitative changes in the transition from one-cell to two-cell structure. For this reason, it is omitted from the force-balance analysis. At low levels, temperature impacts pressure through hydrostatic adjustment; thus, temperature gradients relate to pressure gradients through the hypsometric equation.

This pressure-gradient force is essentially balanced by the combined action of inertial and Coriolis forces. Figure 4 compares the radial profiles of the pressure-gradient force and the sum of the inertial and Coriolis contributions for two values of ΔT_v. Prior to the development of the central downdraft, the pressure-gradient force dominates (Figure 4(A)), creating an inward motion toward the vortex axis. As ΔT_v increases, however, the combined inertial and Coriolis forces overcome the pressure-gradient force, at least for $r < 0.006\,\mathrm{m}$ (Figure 4(B)). Consequently, the inflow is blocked near the axis and a region of descending motion develops and expands along the z-direction, leading to the formation of the two-cell vortex structure.

3.1.2 Intensification of the vortex by condensation

We now examine how the flow structures identified in the dry-air simulations are modified by the presence of moisture and the associated latent heat release due to condensation.

Figure 5(A)-(E) presents the vorticity, temperature, and velocity fields for the single-cell vortex obtained in the moist-air case with $\Delta T_v = 2.25$ K. Overall, the vortex structure is similar to the dry-air case, although some differences arise in the temperature profile as a consequence of

condensation-induced heating near the top of the domain (Figure 5(G)). The imposed initial and boundary conditions are chosen such that the warmer air in the central region is nearly saturated. As this moist air ascends through the vortex core and reaches the cooler upper levels of the domain, it becomes saturated and condensation occurs.

To identify the regions where condensation takes place, Figure 5(F) shows the distribution of $c_v - c_{sat}$, where c_v is the water vapour concentration and c_{sat} is the saturation vapour concentration. Condensation occurs when $c_v - c_{sat} > 0$, as prescribed by the Heaviside functions in Eqs. (5) and (6). Since any condensed liquid water is assumed to be instantaneously removed from the system through precipitation, the vapour concentration rapidly adjusts to its saturation value. Consequently, regions where condensation has occurred appear as zones where $c_v \approx c_{sat}$, corresponding to values close to zero in Figure 5(F). As can be seen, condensation is concentrated in the upper central part of the vortex, where the ascending moist air cools sufficiently to reach saturation. The associated latent heat release generates a localized heat source, as shown in Figure 5(G). This heating enhances the buoyancy of the rising air, strengthening the upward motion relative to the dry-air case and thereby intensifying the single-cell vortex. This effect is evident in the velocity profiles, particularly in the azimuthal velocity component, which exhibits larger values and therefore stronger rotational motion.

Figure 6 illustrates the corresponding moist-air simulation for the two-cell vortex configuration. In this case, condensation takes place within an annular region near the top of the domain (Figure 6(F)), where warm, moisture-laden air, ascending through the outer updraft, reaches saturation. The central hole of this annulus corresponds to the descending cold-air downdraft characteristic of the two-cell vortex, a region in which condensation does not occur. As in the single-cell case, the latent heat released by condensation acts as a localized heat source (Figure 6(G)), promoting upward motion within the condensation region (Figure 6(B)) and contributing to vortex intensification. However, the magnitude of this effect is smaller than that observed in the single-cell vortex. This can be seen by comparing the velocity fields of the dry cases (Figures 2(C)-(E) and 3(C)-(E)) with those of the moist cases (Figures 5(C)-(E) and 6(C)-(E)).

Further insight into the intensification mechanism can be obtained from a radial force balance analysis. Figure 7 shows the radial profiles of the pressure-gradient force, the Coriolis

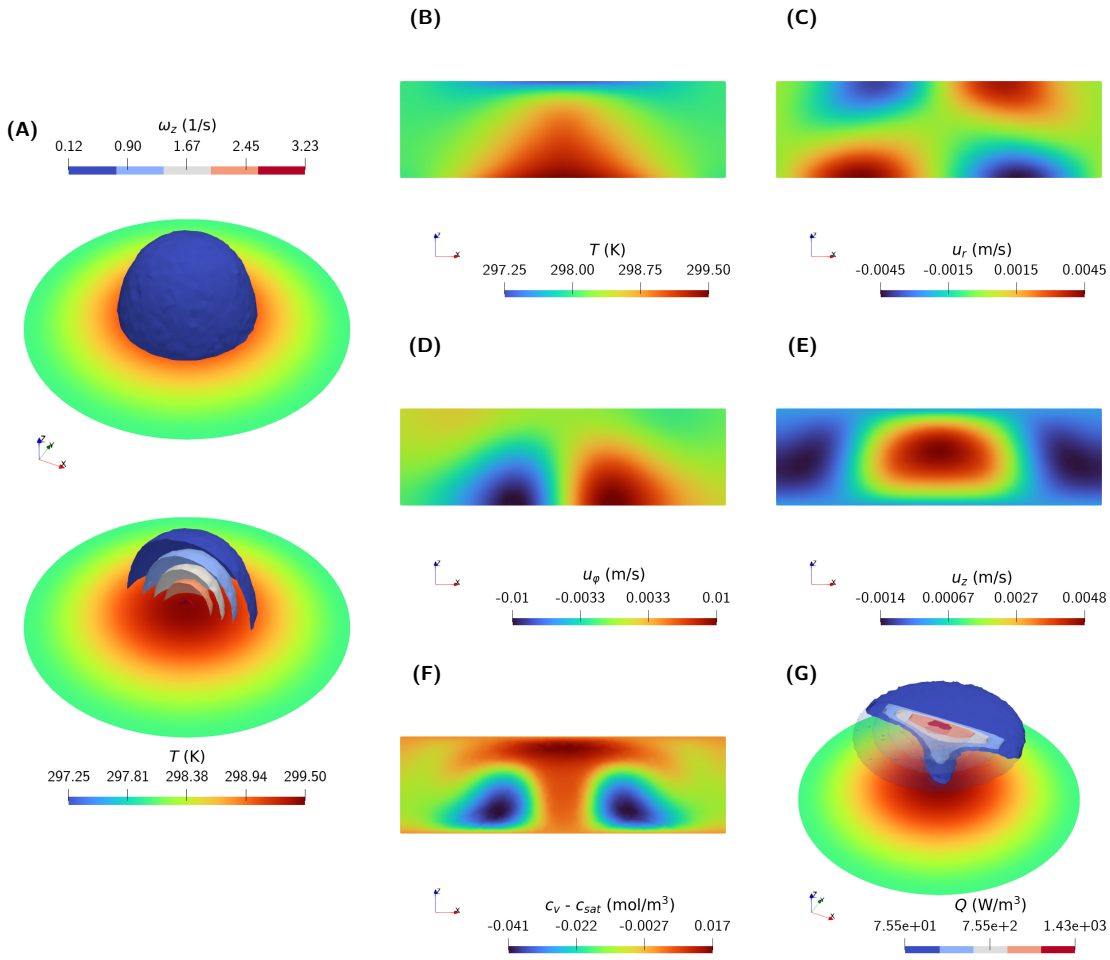

Figure 5: One-cell stationary vortex for the moist case obtained for $\beta_b = 5$, $\Delta T_v = 2.25$ K, $\Omega = 0.4$ rad/s, and $L = 2.5 \times 10^6$ J/kg. Panel (A) shows isosurfaces of the vertical vorticity, ω_z, together with a slice at $z = 0.01d$ of the temperature field. Panels (B)-(F) show slices at $y = 0$ of the temperature field, the radial, azimuthal, and vertical components of the velocity field, and $c_v - c_{\rm sat}$, respectively. Panel (G) shows isosurfaces of the latent heat source, Q, associated with condensation. In panels (B)-(F), the OY axis points inward.

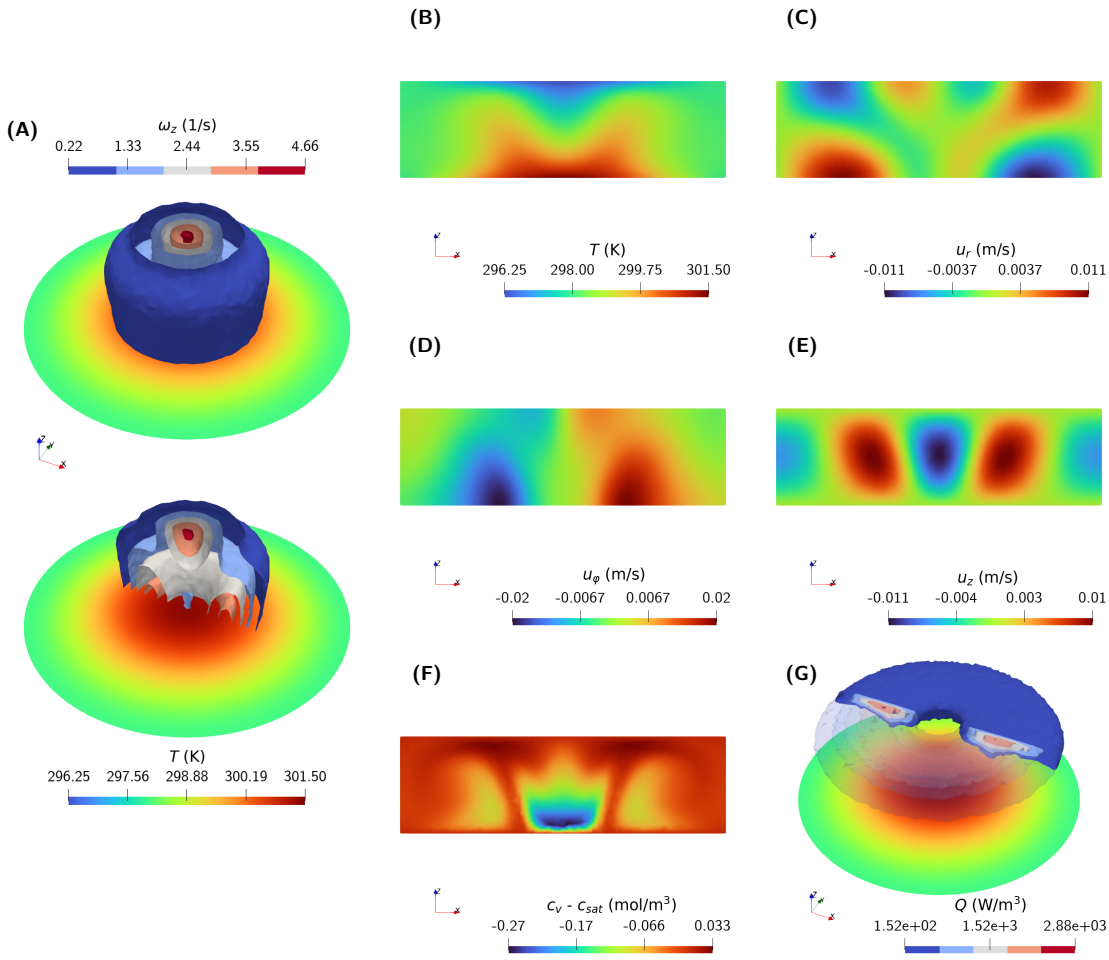

Figure 6: Two-cell stationary vortex for the moist case obtained for $\beta_b = 5$, $\Delta T_v = 5.25$ K, $\Omega = 0.4$ rad/s, and $L = 2.5 \times 10^6$ J/kg. Panel (A) shows isosurfaces of the vertical vorticity, ω_z, together with a slice at $z = 0.01d$ of the temperature field. Panels (B)–(F) show slices at $y = 0$ of the temperature field, the radial, azimuthal, and vertical components of the velocity field, and $c_v - c_{\rm sat}$, respectively. Panel (G) shows isosurfaces of the latent heat source, Q, associated with condensation. In panels (B)–(F), the OY axis points inward.

force, the inertial force, and the sum of the latter two (the viscous force is omitted) at two vertical levels, $z = 0.1d$ and $z = 0.5d$. Results are shown for several values of ΔT_v in both the dry-air case (Figure 7(A)) and the moist-air case (Figure 7(B)).

For $\Delta T_v = 2.25$ K (first row of Figure 7), both the dry and moist simulations exhibit a well-developed single-cell vortex. At both heights, the pressure-gradient force is noticeably stronger in the moist-air case than in the dry-air case, particularly near the vortex core. This enhanced pressure gradient is primarily balanced by the combined inertial and Coriolis forces. Close to the vortex axis, the inertial contribution is dominated by the centrifugal term, $\rho_0 u_\varphi^2/r$ [11]. Consequently, a larger pressure-gradient force requires larger azimuthal velocities to maintain equilibrium, resulting in stronger rotation and a more intense vortex in the moist-air case.

A similar behavior is observed for $\Delta T_v = 5.25$ K (third row of Figure 7), where both simulations produce a fully developed two-cell vortex. Although the enhancement of the pressure-gradient force due to condensation is less pronounced than in the single-cell regime, the moist-air case still exhibits a stronger pressure gradient than the dry-air case. The corresponding increase in the combined inertial and Coriolis forces implies higher azimuthal velocities and therefore stronger rotational motion. These results indicate that condensation intensifies the vortex in both the single-cell and two-cell configurations. We therefore conclude that latent heat release associated with condensation promotes the formation of stronger and more well developed bottom-up vortices.

The intermediate case, $\Delta T_v = 3.5$ K (second row of Figure 7), displays a different behavior. For this parameter setup, the pressure-gradient force is not larger in the moist-air simulation than in the dry-air simulation. This difference arises because the two cases correspond to different vortex structures: the dry-air simulation still exhibits a single-cell vortex, whereas the moist-air simulation has already begun the transition toward a two-cell structure. As known, the transition from a single-cell to a two-cell vortex is accompanied by a reduction in vortex intensity due to a redistribution of angular momentum and kinetic energy within the flow [37].

3.1.3 Variation of ΔT_v including condensation

Figure 8(A) shows the variation of the maximum azimuthal velocity as a function of ΔT_v for both the dry-air and moist-air cases, with $\beta_b = 5$ and $\Omega = 0.4\,\mathrm{rad/s}$. Vertical velocity profiles corresponding to $\Delta T_v = 2.25$, 3.5, and 5.25 K are also included for comparison.

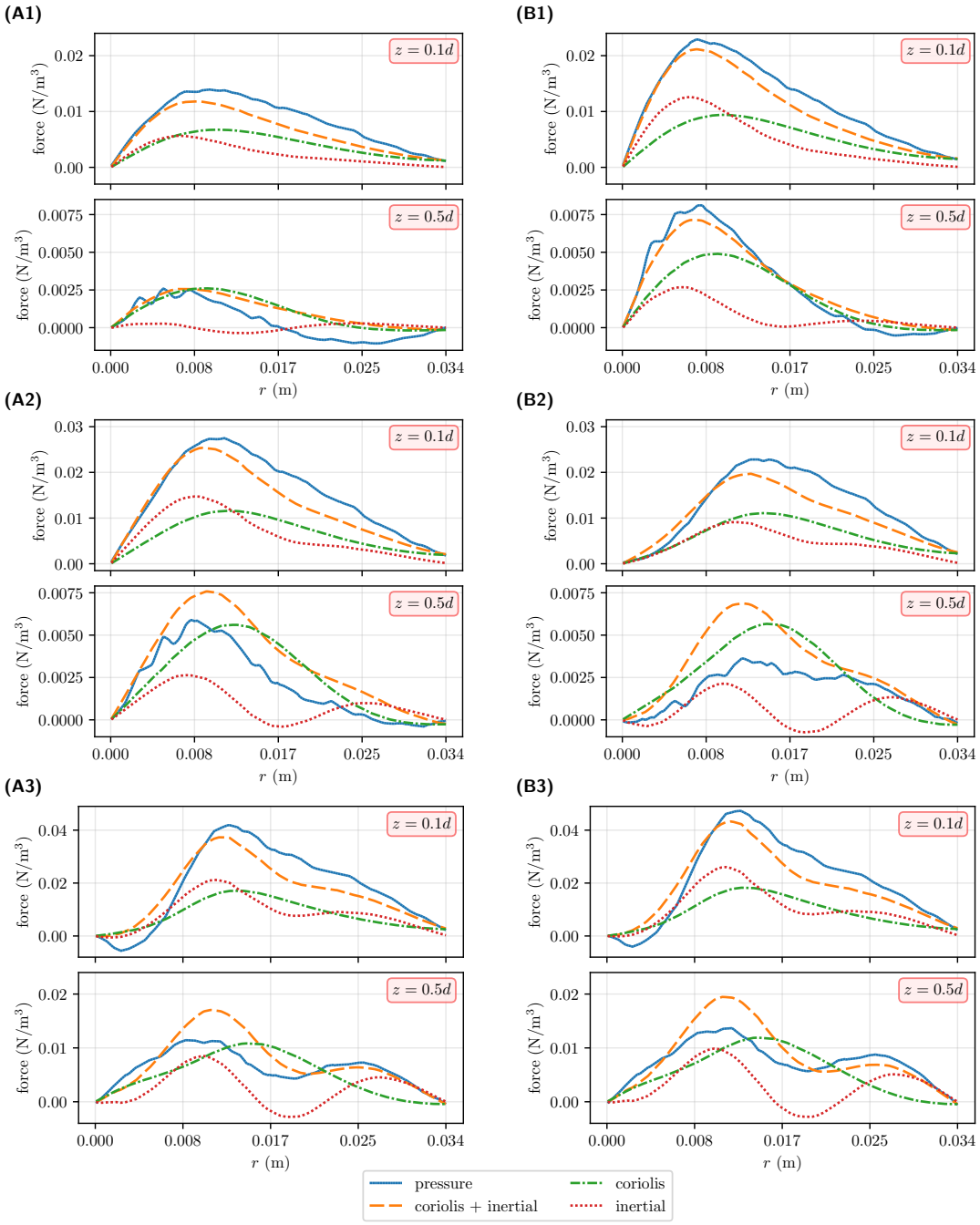

Figure 7: Force balance analysis for stationary vortices obtained with $\beta_b = 5$ and $\Omega = 0.4$ rad/s. Panels (A1)–(A3) correspond to the dry case ($L = 0$ J/kg), whereas panels (B1)–(B3) correspond to the moist case ($L = 2.5 \times 10^6$ J/kg). Rows 1–3 correspond to $\Delta T_v = 2.25$, 3.5, and 5.25 K, respectively. Each panel shows the radial profiles of the pressure gradient, the Coriolis force, the inertial force, and their sum at $z = 0.1d$ (top) and $z = 0.5d$ (bottom).

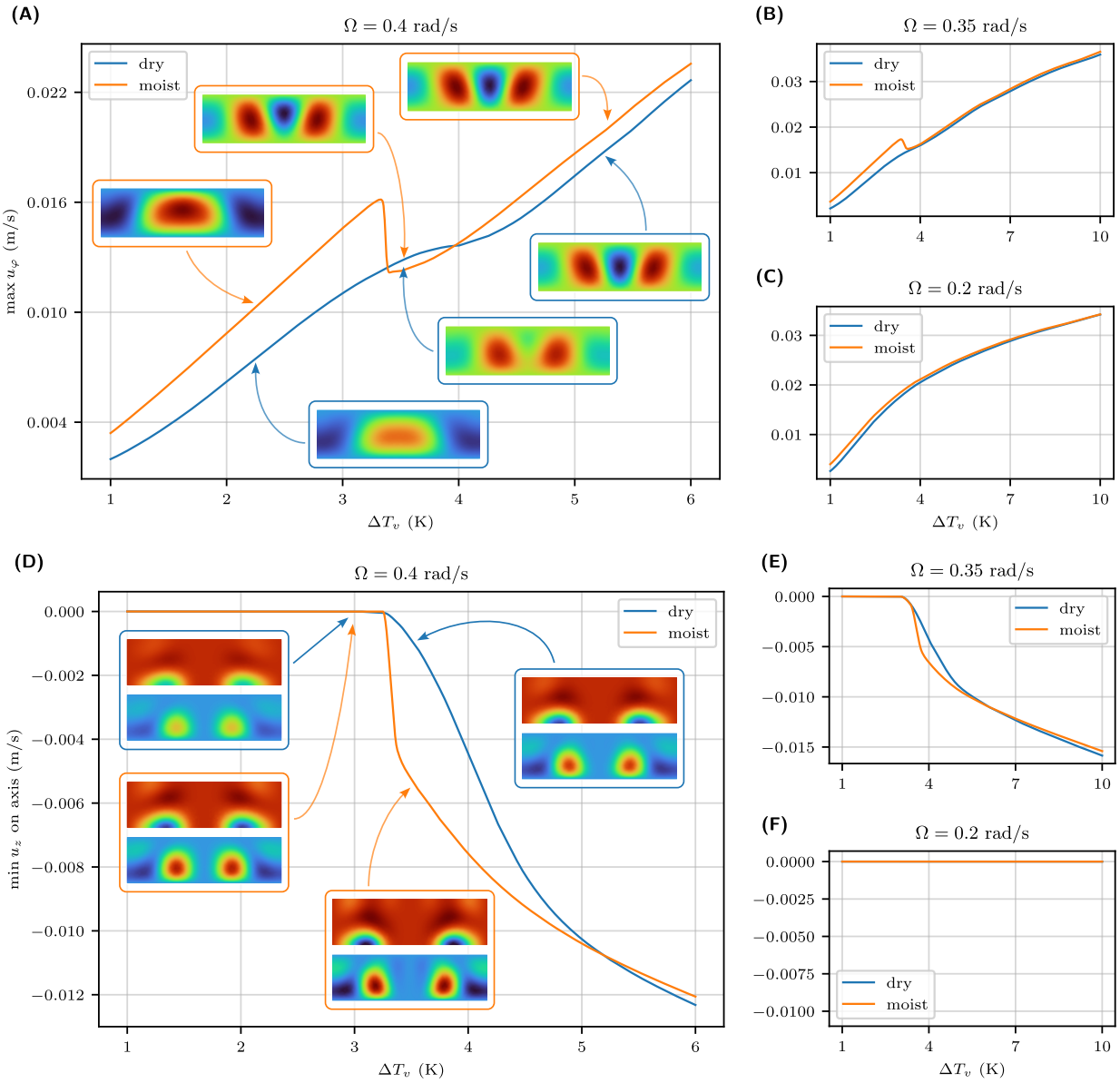

Figure 8: (A) Maximum azimuthal vortex velocity $\max u_\varphi$ as a function of ΔT_v for the dry ($L = 0$ J/kg) and moist ($L = 2.5 \times 10^6$ J/kg) configurations for $\beta_b = 5$, case $\Omega = 0.4$ rad/s. Vertical velocity profiles for the dry and moist cases at $\Delta T_v = 2.25$, 3.5, and 5.25 K are also included. The color scale limits used for the vertical velocity slices are $[-0.0014, 0.0048]$ for $\Delta T_v = 2.25$ K, $[-0.0053, 0.0052]$ for $\Delta T_v = 3.5$ K, and $[-0.011, 0.010]$ for $\Delta T_v = 5.25$ K. (B) Case $\Omega = 0.35$ rad/s. (C) Case $\Omega = 0.2$ rad/s. (D) Minimum value of u_z on the axis as a function of ΔT_v for the dry ($L = 0$ J/kg) and moist ($L = 2.5 \times 10^6$ J/kg) configurations for $\beta_b = 5$, case $\Omega = 0.4$ rad/s. Boxes show profiles of the two components of the angular-momentum flux F_r (up) and F_z (down) at $\Delta T_v = 3$ and 3.5 K. The color scale limits used for F_r are $[-1.4 \times 10^{-6}, 1.9 \times 10^{-7}]$ and for F_z, $[-1.9 \times 10^{-7}, 6.9 \times 10^{-7}]$. (E) Case $\Omega = 0.35$ rad/s. (F) Case $\Omega = 0.2$ rad/s.

As ΔT_v increases, both the dry and moist simulations undergo a transition from a single-cell vortex to a two-cell vortex. However, the nature of this transition differs significantly between the two cases. In the presence of condensation, the transition occurs much more abruptly than in the dry-air case, as evidenced by the vertical velocity profiles.

In the dry model, buoyancy depends exclusively on temperature, and the response of the circulation to increasing ΔT_v is relatively smooth. The strength of the ascending and descending motions increases progressively, and heat redistribution occurs continuously throughout the domain. As a result, the transition from a single-cell to a two-cell circulation typically takes place in a gradual manner.

In the moist simulations, condensation introduces an additional coupling between the flow and the thermal field. As moist air is transported into colder regions of the domain, condensation occurs and latent heat is released. This heating locally increases buoyancy and modifies the circulation, which in turn affects the transport of heat and moisture. The resulting interaction makes the system more sensitive to changes in the control parameters and contributes to the sharper transition observed between the one-cell and two-cell vortex states.

To determine precisely the critical threshold at which the transition from a single-cell vortex to a two-cell vortex occurs we have followed the evolution of the minimum value of u_z along the cylinder axis as ΔT_v is varied for $\beta_b = 5$ and $\Omega = 0.4$ rad/s for both the dry and moist cases (Figure 8(D)). The threshold is reached as the minimum value of u_z along the cylinder axis becomes negative (the downdraft begins to develop). As shown in Figure 8(D) the onset of the single-cell to two-cell transition occurs essentially at the same value of the control parameter ΔT_v in both the dry and moist simulations. However, condensation accelerates the development of the two-cell structure. This effect is clearly visible in the evolution of the minimum axial velocity when comparing the dry and moist simulations. The decrease toward negative values is more abrupt in the moist case than in the dry case. This indicates a more rapid formation of the central downdraft and, consequently, a faster establishment of a fully developed two-cell structure.

The reduction in vortex intensity following the single-cell to two-cell transition observed in Figure 8(A) for the moist case is associated with this faster development of the two-cell structure and how the transport of anular momentum is distributed. In Figure 8(D) contour plots of the

angular-momentum flux components $F_r = \rho r u_r u_\varphi$ and $F_z = \rho r u_z u_\varphi$ are included for values of the control parameter ΔT_v immediately before and immediately after the transition to the two-cell regime.

We start analyzing the angular momentum transport patterns in the dry and moist cases immediately before the transition to the double-cell regime. As observed in Figure 8(D) the radial flux F_r exhibits negative values in the lower part of the domain, indicating inward transport of angular momentum toward the axis in that region. However, a central region of weakened transport develops, which is consistent with the onset of a double-cell structure. A similar signature can be identified in the F_z distribution, which already displays two distinct regions of vertical angular momentum transport separated by a zone of relatively weak flux. This behavior is considerably more pronounced in the moist case than in the dry one, suggesting that moisture promotes a more mature organization of the secondary circulation, compatible with an earlier transition toward a well-developed double-cell structure.

The profiles of the angular momentum flux components after the transition further highlight these differences. In the moist case, the regions with $F_r < 0$ are located at larger radii than in the dry case, indicating the development of a broader downdraft region. Likewise, the region with $F_z > 0$ extends over a larger vertical range, consistent with a more developed double-cell vertical structure. This interpretation is also supported by the larger magnitudes of both $\mid Fr \mid$ and $\mid Fz \mid$ in the moist configuration compared with the dry one.

Overall, the analysis of the angular momentum flux components provides a more detailed view of the important role played by moisture in the establishment and consolidation of the double-cell structure in bottom-up thermoconvective vortices.

When the ambient rotation rate is reduced, the transition becomes noticeably smoother and may eventually disappear. Figure 8(B)-(E) shows that, for lower values of Ω, the change from a single-cell to a two-cell vortex in the moist-air case occurs more gradually. This behavior can be attributed to the weaker influence of the Coriolis force. Under weaker rotational constraints, the redistribution of angular momentum and the reorganization of the flow proceed more progressively, allowing the secondary circulation cell to emerge and expand in a less abrupt manner. As the rotation rate is further decreased, the transition does not occur. Indeed, in Figure 8(C) there is no

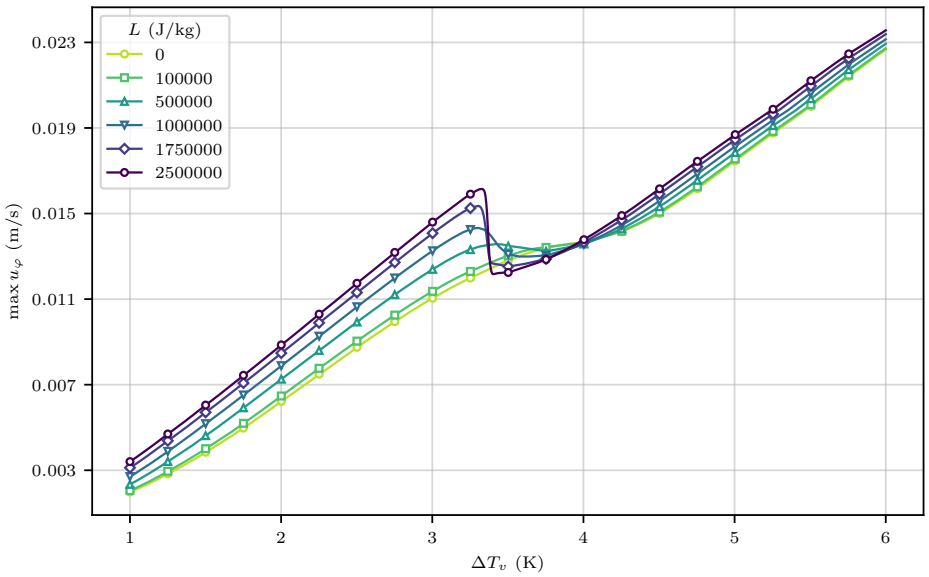

Figure 9: Transition between the dry case, $L = 0$ J/kg and the moist case, $L = 2.5 \times 10^6$ J/kg. The plot shows the maximum azimuthal velocity in the domain, $\max u_\varphi$, as a function of the imposed vertical temperature difference, ΔT_v, for stationary vortices with $\beta_b = 5$ and $\Omega = 0.4$ rad/s.

transition from a single-cell to a two-cell structure within the range of ΔT_v considered, as clearly shown in Figure 8(F).

Figure 9 presents the variation of the maximum azimuthal velocity with ΔT_v for simulations with $\beta_b = 5$ and $\Omega = 0.4$ rad/s in which the latent heat parameter is varied from $L = 2.5 \times 10^6$ J/kg to $L = 0$ J/kg, the latter corresponding to the dry-air case. As expected, decreasing L progressively weakens the effect of condensation, and the resulting solutions approach those of the dry-air simulations.

3.1.4 Variation of β_b including condensation

In this section, simulations were performed for $\Delta T_v = 5$ K and $\Omega = 0.35$ rad/s while varying the thermal parameter β_b, which controls the spatial extent of the Gaussian temperature distribution imposed at the lower boundary. The results are qualitatively similar to those obtained when varying ΔT_v.

Figure 10 compares the dry-air and moist-air simulations. As in the previous section, condensation leads to a clear intensification of the vortex while the flow remains in the single-

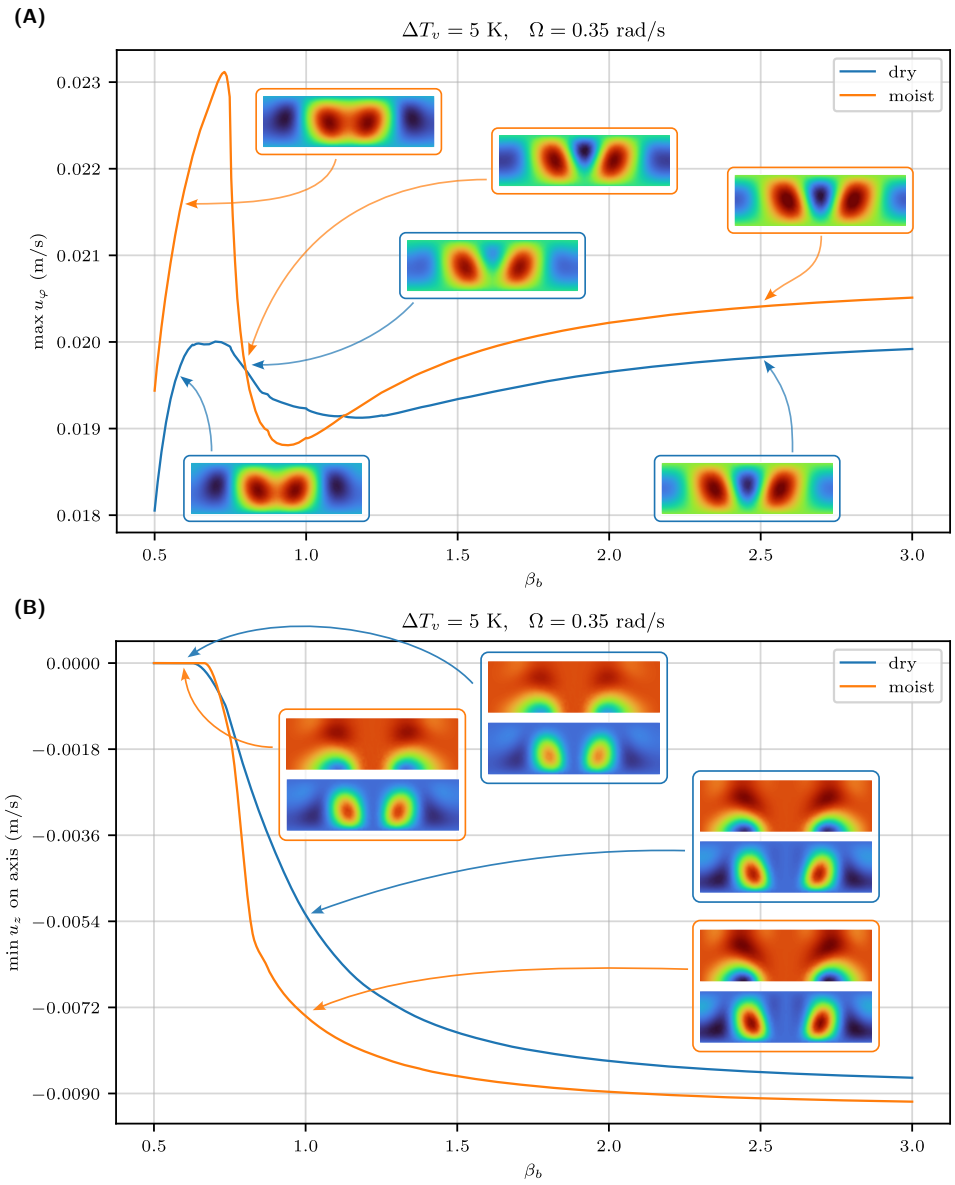

Figure 10: (A) Effect of the bottom heat-source sharpness, β_b, on the maximum azimuthal velocity in the domain, $\max u_\varphi$, for stationary vortices with $\Delta T_v = 5$ K and $\Omega = 0.35$ rad/s. The plot compares the dry ($L = 0$ J/kg) and moist ($L = 2.5 \times 10^6$ J/kg) cases by showing $\max u_\varphi$ as a function of β_b. In addition, slices at $y = 0$ of the vertical velocity are shown for the dry and moist cases at $\beta_b = 0.6$, 0.8, and 2.5. The color scale limits used for the vertical velocity slices are $[-0.0030, 0.0087]$ for $\beta_b = 0.6$, $[-0.0050, 0.0083]$ for $\beta_b = 0.8$, and $[-0.0092, 0.0100]$ for $\beta_b = 2.5$ (B) Minimum value of u_z on the axis as a function of β_b for the dry ($L = 0$ J/kg) and moist ($L = 2.5 \times 10^6$ J/kg) configurations for $\Delta T = 5$ K and $\Omega = 0.35$ rad/s. Boxes show profiles of the two components of the angular-momentum flux F_r (up) and F_z (down) at $\beta_b = 0.625$ and $\beta_b = 1$. The color scale limits used for F_r are $[-2.7 \times 10^{-6},\ 6.4 \times 10^{-7}]$ and for F_z, $[-3 \times 10^{-7},\ 1.8 \times 10^{-6}]$.

cell regime ($\beta_b < 0.7$). As β_b increases, a more abrupt transition from a single-cell to a two-cell vortex occurs in the moist-air case (Figure 10(B)), as revealed by the angular momentum transport patterns, accompanied by a reduction in vortex intensity (Figure 10(A)) associated with the reorganization of the flow structure. For $\beta_b > 1.15$, where a fully developed two-cell vortex is established in both the dry and moist cases, the moist-air vortex again becomes more intense than its dry-air counterpart.

The physical explanation of the transition from the single-cell to the two-cell regime is analogous to that described in Section 3.1.1 for variations of ΔT_v, and therefore a detailed discussion is omitted here.

3.1.5 Variation of Ω including condensation

We now investigate the influence of ambient rotation on the intensification of thermoconvective vortices under both dry and moist conditions. Figure 11(A) shows the variation of the maximum azimuthal velocity with the ambient rotation rate Ω for simulations with $\beta_b = 5$ and $\Delta T_v = 3.5$ K. The corresponding vertical velocity profiles for $\Omega = 0.167$, 0.30, and 0.50 rad/s are also presented for both the dry-air and moist-air cases.

As expected, increasing the ambient rotation promotes the transition from a single-cell vortex to a two-cell vortex [9]. However the behavior is different from that of the configurations when the control parameter is a thermal parameter (ΔT_v or β_b) as analysed in previous sections.

Although moisture ultimately promotes the establishment of a more developed double-cell structure, it also appears to increase the robustness of the single-cell regime (Figures 11(A)-(D)). Latent heat release strengthens the primary thermoconvective circulation and enhances angular momentum transport, allowing the single-cell vortex to remain stable over a wider range of rotation rates. As a result, the onset of the single-cell to double-cell transition is shifted to slightly larger values of Ω in the moist case. Once the transition takes place, however, the resulting double-cell structure is more clearly established, as indicated by the stronger and more spatially extended angular momentum fluxes F_r and F_z (Figure 11(D)).

In the case of increasing background rotation, the angular-momentum flux evolves more gradually than when thermal parameters are varied. This suggests that the vortex adjusts through a progressive redistribution of angular momentum as the background rotation increases. As a result,

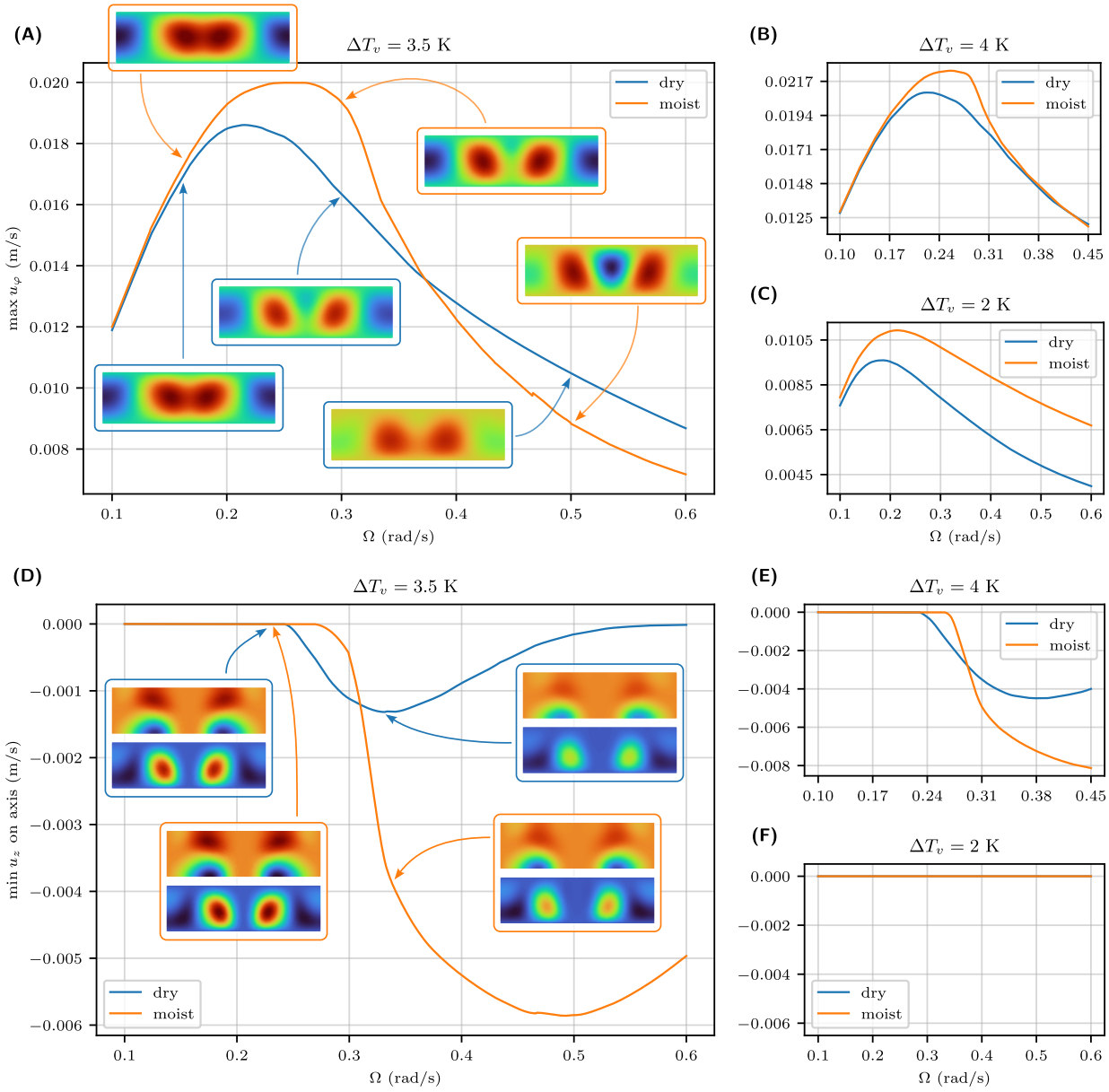

Figure 11: (A) Relationship between the ambient rotation rate, Ω, and the maximum azimuthal velocity in the domain, $\max u_\varphi$, for stationary vortices with $\beta_b = 5$. Panels (A)–(C) compare the dry ($L = 0$ J/kg) and moist ($L = 2.5 \times 10^6$ J/kg) cases for $\Delta T_v = 3.5$, 4, and 2 K, respectively, by showing $\max u_\varphi$ as a function of Ω. In addition, panel (A) includes slices at $y = 0$ of the vertical velocity for the dry and moist cases at $\Omega = 0.167$, 0.3, and 0.5 rad/s. The color scale limits used for the vertical velocity slices are $[-0.007, 0.013]$ for $\Omega = 0.167$ rad/s, $[-0.0050, 0.0082]$ for $\Omega = 0.3$ rad/s, and $[-0.006, 0.004]$ for $\Omega = 0.5$ rad/s. (D) Minimum value of u_z on the axis as a function of Ω for the dry ($L = 0$ J/kg) and moist ($L = 2.5 \times 10^6$ J/kg) configurations for $\Delta T = 3.5$ K and $\beta_b = 5$. Boxes show profiles of the two components of the angular-momentum flux F_r (up) and F_z (down) at $\Omega = 0.23$ and $\Omega = 0.3$ rad/s. The color scale limits used for F_r are $[-2.3 \times 10^{-6},\ 8.8 \times 10^{-7}]$ and for F_z, $[-2.3 \times 10^{-7},\ 1.8 \times 10^{-6}]$. (E) Case $\Delta T = 4$ K; (F) Case $\Delta T = 2$ K.

the decrease in vortex intensity is smoother than that observed in thermally forced transitions, where changes in buoyancy can produce a more abrupt reorganization of the secondary circulation and the associated transport of angular momentum.

For larger values of ΔT_v, these differences between the dry and moist cases in the consolidation of the two-cell structure as Ω increases become less pronounced (Figures 11(B)-(E)). For smaller values of ΔT_v, both the dry and moist configurations remain in the single-cell regime despite the increase in Ω, as shown in Figures 11(C)-(F) for $\Delta T_v = 2$ K.

The results also show that moist single-cell thermoconvective vortices are more intense than their dry-air counterparts as the ambient rotation increases. This behavior can be observed in Figure 11(A) for $\Omega < 0.26$, in Figure 11(B) for $\Omega < 0.28$, and throughout the range shown in Figure 11(C). The enhanced intensity arises from the latent heat released in the upper central region of the vortex, where condensation occurs (Figure 5(G)). This localized heating acts as an additional buoyancy source within the updraft, favoring the intensification of the vortex circulation.

3.2 Case 2: Top-down vortices

In this section, we consider a different flow configuration, namely top-down forming vortices. These structures are obtained by imposing a larger horizontal thermal gradient at the top than at the bottom of the cylinder. In particular, in the following numerical simulations, we set $\delta^u = -2/3$ and $\delta^b = 1/3$. Throughout this section, the thermal localization parameters are fixed at $\beta_u = \beta_b = 5$.

3.2.1 Weaker moist top-down vortex

Figure 12 compares the maximum azimuthal velocities obtained for the dry-air and moist-air top-down vortices as a function of the imposed vertical temperature difference. In this simulation the ambient rotation rate is fixed to $\Omega = 0.3$ rad/s. Unlike the bottom-up configuration, the dry vortex is more intense than the moist vortex over the entire range of ΔT_v considered. The differences are relatively small within the single-cell regime, as illustrated by the case $\Delta T_v = 2$ K, but become considerably more pronounced once the flow transitions to a two-cell structure, as observed for $\Delta T_v = 6$ K.

As in the bottom-up configuration, the transition from a single-cell to a two-cell vortex is more abrupt in the presence of moisture. However, a notable difference emerges: in the top-down

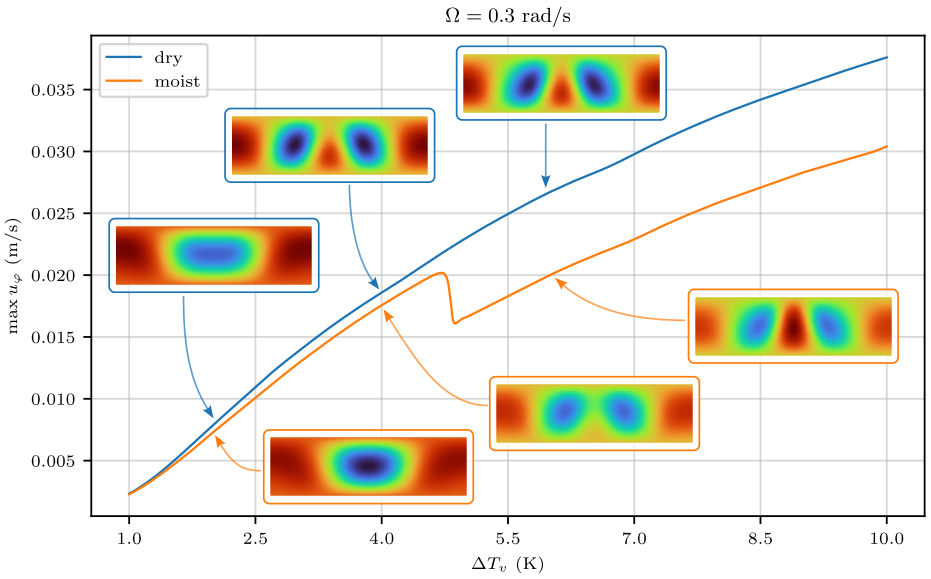

Figure 12: Relationship between the imposed vertical temperature difference, ΔT_v, and the maximum azimuthal velocity in the domain, $\max u_\varphi$, for stationary top-down vortices with $\beta_b = \beta_u = 5$ and $\Omega = 0.3$ rad/s. The plot compares the dry ($L = 0$ J/kg) and moist ($L = 2.5 \times 10^6$ J/kg) cases by showing $\max u_\varphi$ as a function of ΔT_v. In addition, slices at $y = 0$ of the vertical velocity are included for the dry and wet cases at $\Delta T_v = 2$, 4, and 6 K. The color scale limits used for the vertical velocity slices are $[-0.0051, 0.0014]$ for $\Delta T_v = 2$ K, $[-0.0088, 0.0051]$ for $\Delta T_v = 4$ K, and $[-0.016, 0.011]$ for $\Delta T_v = 6$ K.

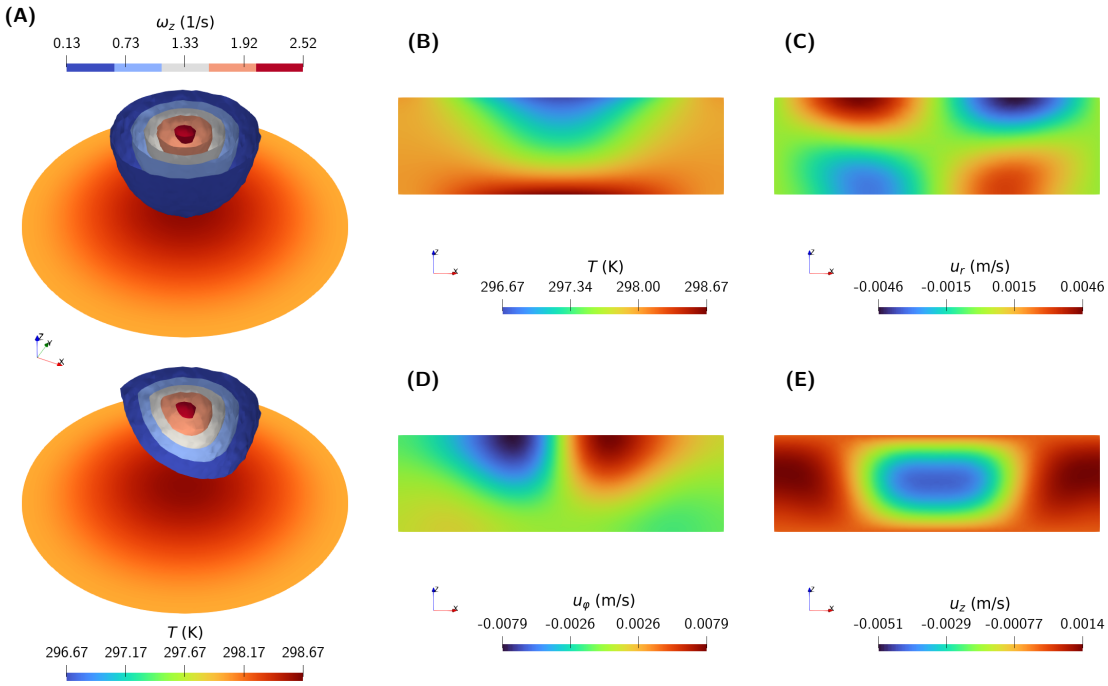

Figure 13: Stationary top-down vortex obtained for $\Delta T_v = 2$ K, $\Omega = 0.3$ rad/s, and $L = 0$ J/kg. Panel (A) shows isosurfaces of the vertical vorticity, ω_z, together with a slice at $z = 0.01d$ of the temperature field. Panels (B)–(E) show slices at $y = 0$ of the temperature field and the radial, azimuthal, and vertical components of the velocity field, respectively. In panels (B)-(E), the OY axis points inward.

configuration, the transition occurs at a lower value of ΔT_v in the dry-air case than in the moist-air case, which is the opposite of the behavior observed for bottom-up vortices. To understand these differences, we compare the dry and moist solutions in both flow regimes. We begin with the single-cell vortex. Figure 13 shows the vorticity, temperature, and velocity fields for the dry-air case with $\Delta T_v = 2$ K and $\Omega = 0.3$ rad/s. Whereas, Figure 14 presents the corresponding moist-air solution together with the distributions of $c_v - c_{\text{sat}}$ and the latent heat source term, Q.

As shown in Figure 13, the strong horizontal temperature gradient near the upper boundary generates a radial pressure gradient that drives the flow inward toward the cylinder axis. This behavior is clearly visible in the radial velocity field. Upon reaching the central region, the fluid descends while rotating around the axis, producing the characteristic top-down vortex structure evidenced by the vertical and azimuthal velocity components.

In the moist-air case (Figure 14), condensation occurs as the air moves from the relatively warm outer region of the upper layer toward the colder central region. The latent heat released during condensation contributes to the formation of a stronger radial pressure gradient, as shown in Figure 15(A_1–B_1). As a result, the inward radial velocity increases, the descending motion becomes stronger, and the vortex core becomes slightly narrower. However, these structural changes produce only minor differences in the maximum azimuthal velocity, which explains the close agreement between the dry and moist solutions observed in Figure 12 within the single-cell regime.

We now analyse the two-cell top-down vortex case. Figures 16 and 17 present the dry-air and moist-air solutions, respectively, for $\Delta T_v = 6$ K and $\Omega = 0.3$ rad/s.

The results in Figure 16 show that, the dry-air vortex develops a tongue of warm air that rises along the cylinder axis, revealing the central updraft characteristic of the two-cell structure. Regarding the moist-air case, and, in contrast to the single-cell regime, the region of maximum condensation is no longer located near the upper part of the vortex. Instead, condensation occurs primarily along the cylinder axis, where the ascending warm, moisture-laden air encounters cooler surroundings and reaches saturation. As a consequence, latent heat is released mainly in the central updraft region, as illustrated in Figure 17. The associated heating significantly modifies the vortex structure. In particular, the central warm-air tongue becomes more pronounced and extends to higher elevations, warming the colder air in the upper part of the domain. This alteration of

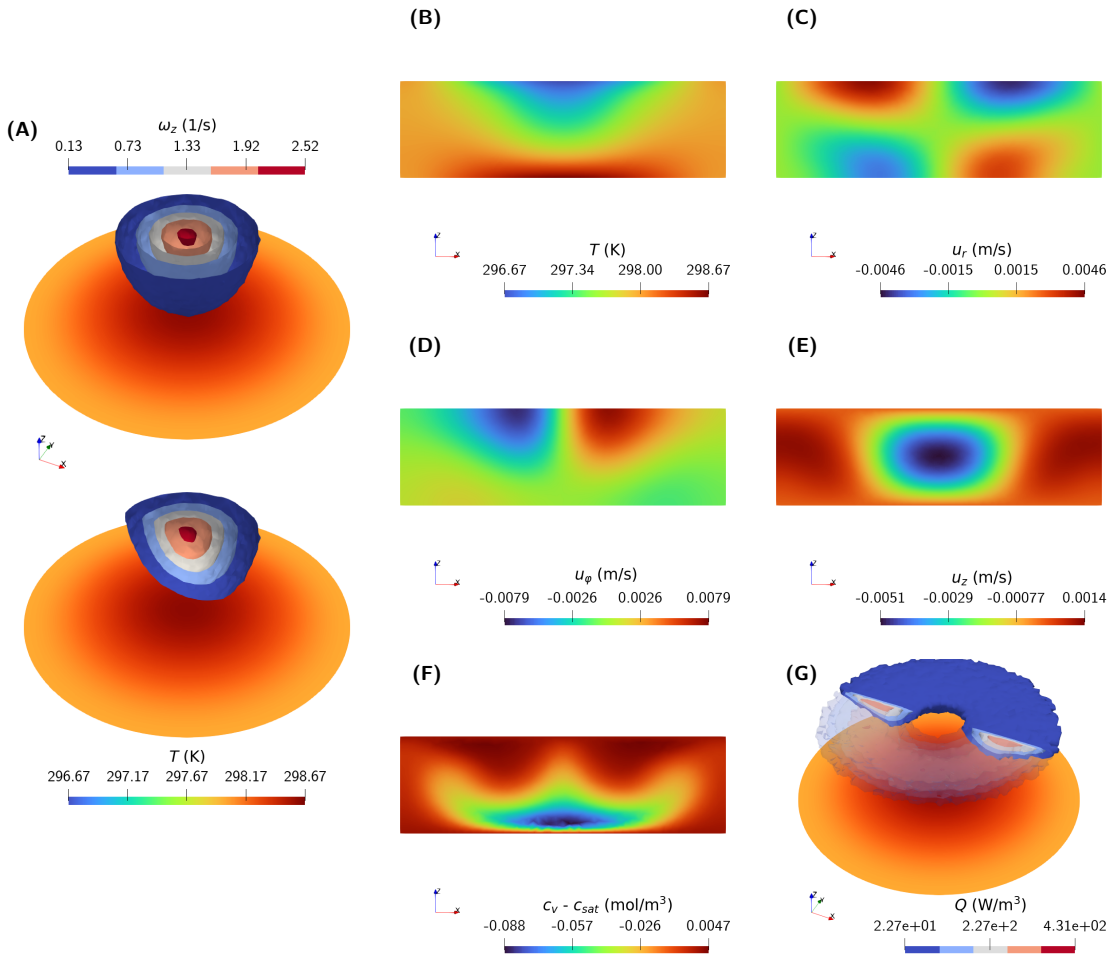

Figure 14: Stationary top-down vortex obtained for $\Delta T_v = 2$ K, $\Omega = 0.3$ rad/s, and $L = 2.5 \times 10^6$ J/kg. Panel (A) shows isosurfaces of the vertical vorticity, ω_z, together with a slice at $z = 0.01d$ of the temperature field. Panels (B)–(F) show slices at $y = 0$ of the temperature field, the radial, azimuthal, and vertical components of the velocity field, and the supersaturation field, $c_v - c_{\text{sat}}$, respectively. Panel (G) shows isosurfaces of the latent heat source, Q, associated with condensation. In panels (B)–(F), the OY axis points inward.

the thermal field produces a broader vortex, as evidenced by the azimuthal velocity distribution. However, despite its larger spatial extent, the vortex exhibits a weaker rotational intensity than in the dry-air case.

Condensation therefore has a predominantly morphological effect in this regime. Rather than strengthening the vortex circulation, the latent heat release modifies the flow structure and redistributes the thermal field in a manner that reduces the vortex intensity. This reduction is clearly visible in Figure 12 for $\Delta T_v = 6$ K.

The force-balance analysis supports this interpretation. As shown in Figures 15(A_3) and 15(B_3), the radial pressure-gradient force is stronger in the dry-air vortex than in the moist-air vortex. Consequently, the combined inertial and Coriolis forces required to balance the pressure gradient are also larger in the dry case. Since these forces are directly related to the magnitude of the azimuthal velocity [11], the weaker pressure gradient in the moist-air vortex leads to a reduction in rotational intensity, consistent with the velocity profiles shown previously.

Figures 15(A_2) and 15(B_2) show an intermediate case corresponding to $\Delta T_v = 4$ K, for which the vortex is undergoing the transition from a single-cell to a two-cell structure. At this stage, the differences between the dry-air and moist-air solutions remain relatively small. As a result, the differences in vortex intensity are also small, consistent with the trends observed in Figure 12.

3.2.2 Effect of Ω in moist top-down vortex

When analyzing the influence of ambient rotation on dry and moist top-down vortices, different behaviors arise depending on the imposed vertical temperature difference, ΔT_v. Figure 18 shows the variation of the maximum azimuthal velocity with the ambient rotation rate, together with the corresponding transitions from single-cell to two-cell vortex structures, for two representative values of ΔT_v.

For $\Delta T_v = 6$ K (Figure 18(B)), the dry-air vortices are consistently more intense than the moist-air vortices over the entire range of rotation rates considered. The difference becomes particularly pronounced when the moist-air vortex undergoes an abrupt transition from a single-cell to a two-cell structure. A different behavior is observed for $\Delta T_v = 4$ K (Figure 18(A)). In this case, the moist-air simulations do not exhibit a single-cell to double-cell transition for the range

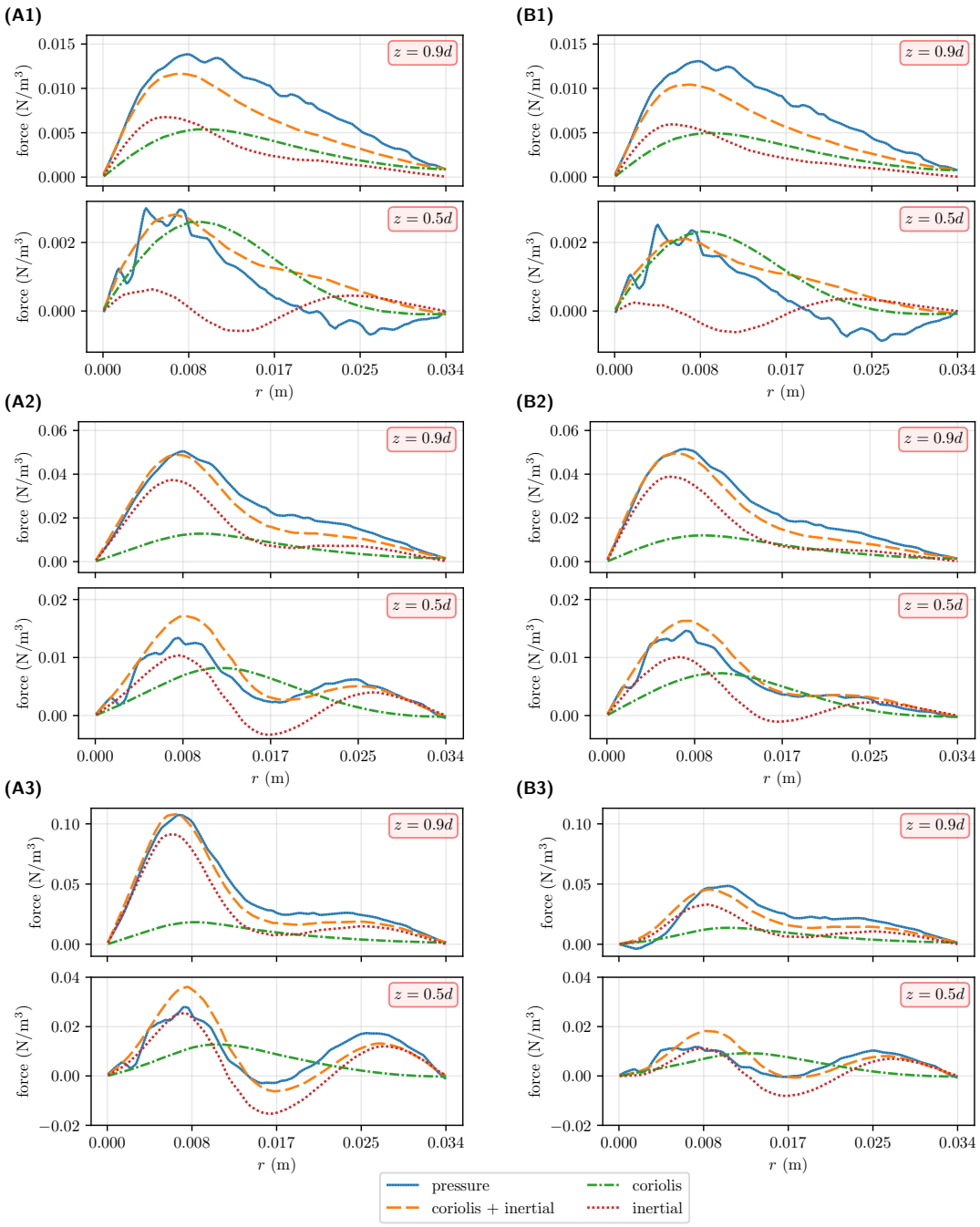

Figure 15: Force balance for top-down stationary vortices obtained with $\Omega = 0.3$ rad/s. Panels (A1)–(A3) correspond to the dry case ($L = 0$ J/kg), whereas panels (B1)–(B3) correspond to the moist case ($L = 2.5 \times 10^6$ J/kg). Rows 1–3 correspond to $\Delta T_v = 2$, 4, and 6 K, respectively. Each panel shows the radial profiles of the pressure gradient, the Coriolis force, the inertial force, and their sum at $z = 0.9d$ (top) and $z = 0.5d$ (bottom).

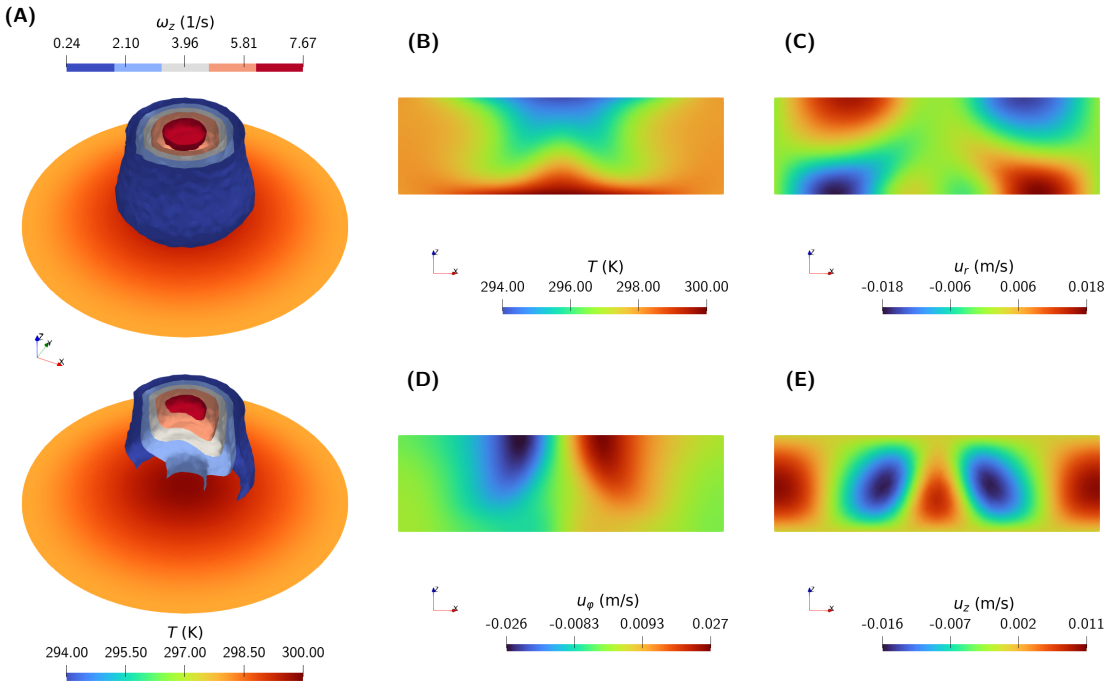

Figure 16: Stationary top-down vortex obtained for $\Delta T_v = 6$ K, $\Omega = 0.3$ rad/s, and $L = 0$ J/kg. Panel (A) shows isosurfaces of the vertical vorticity, ω_z, together with a slice at $z = 0.01d$ of the temperature field. Panels (B)–(E) show slices at $y = 0$ of the temperature field and the radial, azimuthal, and vertical components of the velocity field, respectively. In panels (B)-(E), the OY axis points inward.

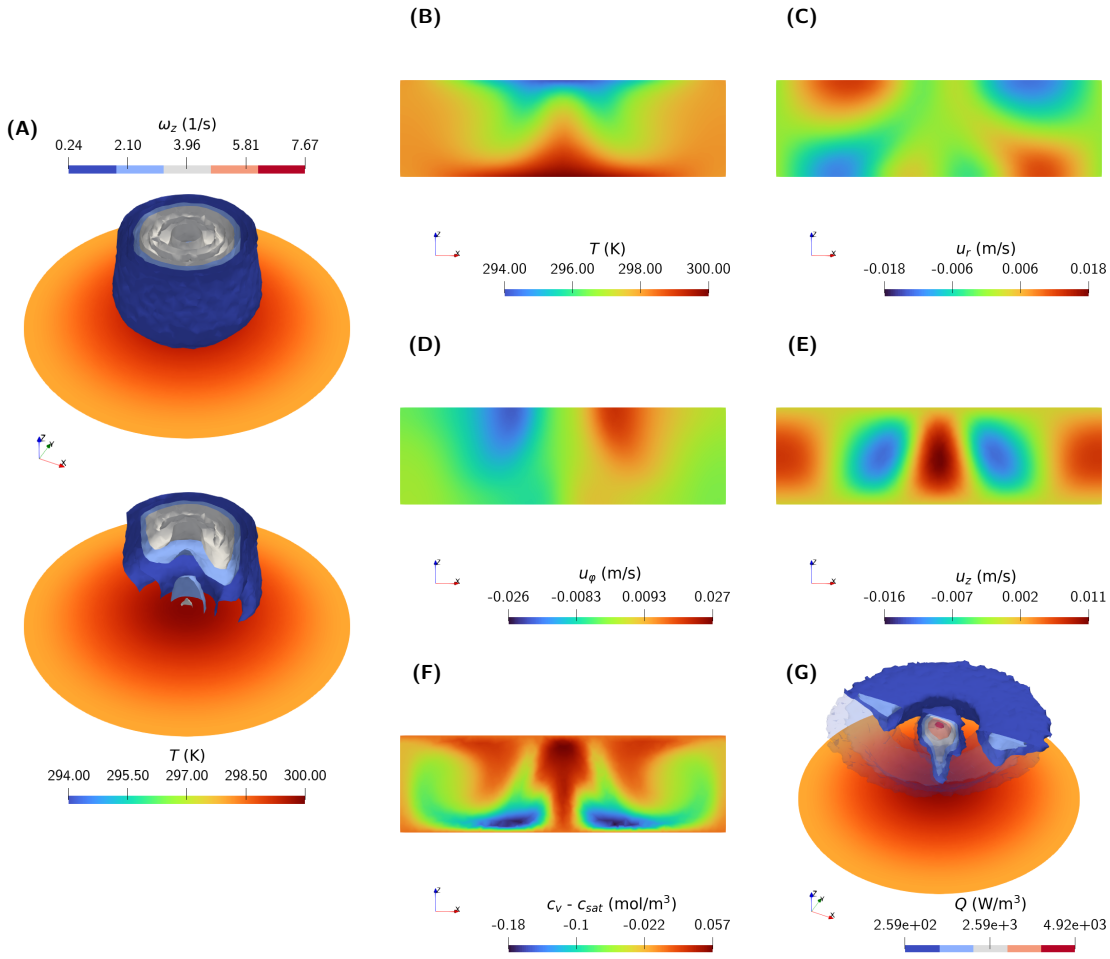

Figure 17: Stationary top-down vortex obtained for $\Delta T_v = 6$ K, $\Omega = 0.3$ rad/s, and $L = 2.5 \times 10^6$ J/kg. Panel (A) shows isosurfaces of the vertical vorticity, ω_z, together with a slice at $z = 0.01d$ of the temperature field. Panels (B)–(F) show slices at $y = 0$ of the temperature field, the radial, azimuthal, and vertical components of the velocity field, and the supersaturation field, $c_v - c_{\text{sat}}$, respectively. Panel (G) shows isosurfaces of the latent heat source, Q, associated with condensation. In panels (B)–(F), the OY axis points inward.

of rotation rates considered in the simulations. As a consequence, there exists a range of rotation rates ($\Omega > 0.36$ rad/s) for which the moist-air vortex remains in the single-cell regime while the dry-air vortex has already undergone the transition to a two-cell configuration. Since the single-cell structure is generally associated with stronger rotational velocities, the moist-air vortex can, in this parameter range, attain higher azimuthal velocities than its dry-air counterpart.

4 Conclusions

In this work, we investigated the effect of condensation on the morphology and intensity of thermo-convective vortices generated by localized cooling and heating at the top and bottom boundaries of a rotating domain. The resulting horizontal and vertical temperature gradients drive the flow into a vortex motion, that can be described as bottom-up or top-down depending of which thermal inhomogeneity dominates. The condensation process we include introduces an additional source of thermal energy through latent heat release. The numerical simulations presented in this work employ the fast-condensation-limit model of [22, 23], which assumes that all condensed moisture is instantaneously removed from the system. This approach avoids the need for more complex two-phase moisture formulations. The vortex model considered here is intentionally idealized and focuses on developed thermoconvective vortices in a small, idealised domain scenario. The goal of the present work is not to reproduce atmospheric vortices quantitatively, but rather to isolate the physical consequences of latent-heat release on a rotating thermoconvective flow. Although the model neglects several processes that are important in the atmosphere, including turbulence, virtual-temperature effects, condensate loading, and adiabatic cooling, it retains the fundamental coupling between buoyancy generation, radial inflow, vertical motion, and vortex circulation.

From this perspective, we believe that the most relevant outcome of the study is not the quantitative prediction of vortex properties but the identification of how condensation modifies the organization of the flow. In particular, the results show that latent-heat release can alter the balance between buoyancy-driven ascent and rotational effects, thereby shifting the transition between one-cell and two-cell vortices. This finding suggests that moisture may influence not only vortex intensity, but also vortex structure and flow topology.

A direct comparison between dry-air and moist-air simulations was performed for both bottom-up and top-down formation vortices. For bottom-up vortices, condensation was found to occur predominantly in the upper region of the domain, where ascending warm air reaches saturation. The resulting latent heat release strengthens the buoyancy-driven circulation and generally promotes an earlier transition from a single-cell to a two-cell vortex compared with the dry-air case. Moreover, the moist-air vortices consistently exhibit stronger rotational motion than their dry-air counterparts. These results demonstrate that condensation favors the formation of

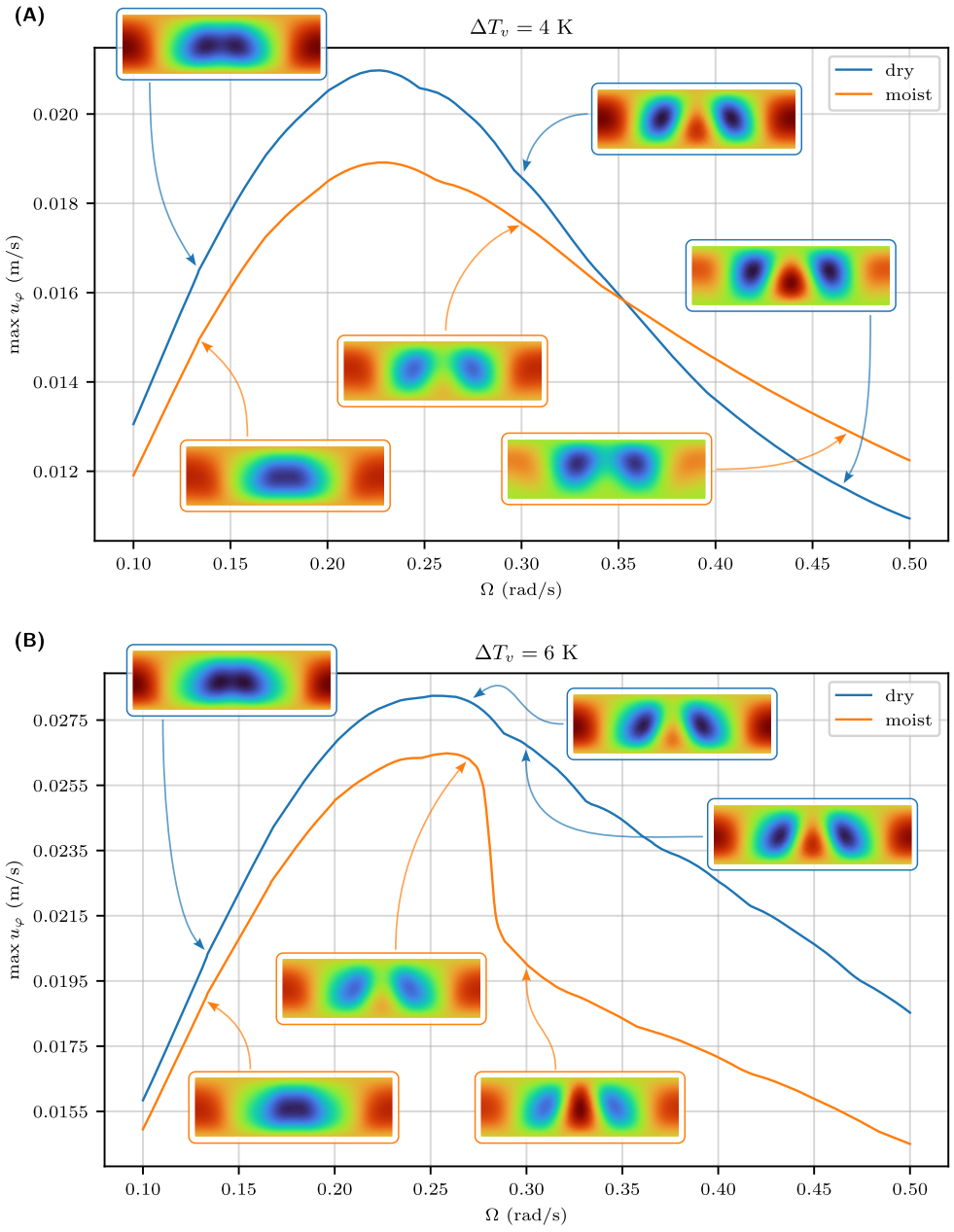

Figure 18: Relationship between the ambient rotation rate, Ω, and the maximum azimuthal velocity in the domain, $\max u_\varphi$, for stationary top-down vortices with $\beta_b = 5$. Panels (A) and (B) compare the dry ($L = 0$ J/kg) and moist ($L = 2.5 \times 10^6$ J/kg) cases for $\Delta T_v = 4$, and 6 K, respectively, by showing $\max u_\varphi$ as a function of Ω. In addition, both panels include slices at $y = 0$ of the vertical velocity for the dry and moist cases at $\Omega = 0.133$, 0.3, and 0.467 rad/s (panel (A)) and $\Omega = 0.133$, 0.267, and 0.3 rad/s (panel (B)). In panel (A), the color scale limits used for the vertical velocity slices are $[-0.0170, 0.0083]$ for $\Omega = 0.133$ rad/s, $[-0.0088, 0.0051]$ for $\Omega = 0.3$ rad/s, and $[-0.0041, 0.0038]$ for $\Omega = 0.467$ rad/s. In panel (B), the color scale limits used for the vertical velocity slices are $[-0.023, 0.013]$ for $\Omega = 0.133$ rad/s, $[-0.017, 0.011]$ for $\Omega = 0.267$ rad/s, and $[-0.016, 0.011]$ for $\Omega = 0.3$ rad/s.

more intense and better-developed bottom-up vortices. The effect of condensation on top-down vortices is markedly different. In this configuration, latent heat release primarily modifies the thermal structure and morphology of the vortex rather than enhancing its rotational intensity. In many cases, condensation delays the transition from the single-cell to the two-cell regime and leads to broader, but dynamically weaker, vortex structures. Consequently, moist top-down vortices are generally less intense than the corresponding dry-air vortices.

The one-cell/two-cell transition is a generic feature observed in many rotating convective vortices, ranging from idealized laboratory and numerical vortices to larger atmospheric systems. Therefore, the finding that condensation changes the location of this transition points to a potentially general mechanism through which moisture can affect vortex dynamics. More broadly, the present simulations isolate the direct dynamical impact of latent heating, which is difficult to extract from atmospheric observations or comprehensive numerical models because many physical processes act simultaneously. By identifying causal relationships between condensation, buoyancy production, and vortex structure, the results provide a simplified conceptual framework that may help interpret the behavior of more realistic moist atmospheric vortices.

A natural extension of the present work is to investigate the effect of condensation on other transitions of the considered system. Previous studies [9, 10] have shown that bifurcations from axisymmetric vortices to asymmetric and chaotic flow states occur in the dry-air case as the governing parameters are varied. Our results indicate that the single-cell to two-cell transition persists in the presence of moisture, although its location in parameter space may be significantly shifted. An important question is therefore whether other bifurcations identified in the dry-air case are similarly displaced, modified, or even suppressed by condensation. Equally intriguing is the possibility that latent heat release could lead to new dynamical regimes that do not exist in dry-air vortices. Addressing these questions could provide a deeper understanding of the role of moisture in the stability and evolution of thermoconvective vortices.

Acknowledgements

This work was partially supported by the Research Grant PID2023-152004NB-I00 (MICIU/AEI/10.13039/501100011033, Spanish Government), and the Research Grant 2025-GRIN-

38610 (Universidad de Castilla-La Mancha), which include ERDF funds. MRT acknowledges the financial support of the Engineering and Physical Sciences Research Council via grant numbers EP/W006545/1 and UKRI070.

For the purpose of open access, the authors have applied a Creative Commons attribution license (CC BY) to any Author Accepted Manuscript version arising from this submission.

Declaration of competing interest

The authors declare that they have no known competing financial interests or personal relationships that could have appeared to influence the work reported in this paper.

Data availability

The data that support the findings of this study are available from the corresponding author upon reasonable request.

A Convergence study of the numerical scheme

We have performed a convergence study of the numerical scheme by increasing the number of elements in the mesh. We have performed the analysis for two different bottom-up vortices configurations, one corresponding to a fully developed two-cell structure in the case of a extended heating profile at the bottom ($\beta_b = 5$) and one corresponding to an emerging double-cell structure, for a localized heating profile at the bottom ($\beta_b = 0.8$). We show a convergence study for both the dry and moist cases.

The results for the two-cell structure in the case of a extended heating profile at the bottom are shown in Figure 19 for $\beta_u = \beta_b = 5$, $\Delta T_v = 6$ K, $\delta^u = -1/3$, $\delta^b = 2/3$ and $\Omega = 0.35$ rad/s. Panels (A) and (B) correspond to the dry case ($L = 0$ J/kg), while panels (C) and (D) correspond to the moist case ($L = 2.5 \times 10^6$ J/kg). Panels (A) and (C) show the temporal evolution of the maximum azimuthal velocity, u_φ, in the domain for three computational meshes with 89 466, 177 144, and 518 040 degrees of freedom (dof). Panels (B) and (D) show clipped isosurfaces of the vertical vorticity together with a temperature slice at $z = 0.01d$ for the stationary solutions obtained on the different meshes.

The results for the incipient two-cell structure in the case of a localized heating profile at the bottom are shown in Figure 20 for $\beta_u = 5$, $\beta_b = 0.8$, $\Delta T_v = 5$ K, $\delta^u = -1/3$, $\delta^b = 2/3$ and $\Omega = 0.35$ rad/s. Panels (A) and (B) correspond to the dry configuration ($L = 0$ J/kg), while panels (C) and (D) correspond to the moist configuration ($L = 2.5 \times 10^6$ J/kg). The temporal evolution of the domain-wide maximum azimuthal velocity, u_φ, is shown in panels (A) and (C) for three meshes with 89 466, 177 144, and 518 040 degrees of freedom (dof). Panels (B) and (D) depict clipped vertical-vorticity isosurfaces and a temperature slice at $z = 0.01d$ for the corresponding stationary states computed on each mesh.

As observed, we obtain very good qualitative and quantitative agreement with all three meshes in both cases, dry and moist air, for both configurations. For the results in the study we have chosen the mesh with 177 144 dof, which gives converged results, but also balances the need for moderate computation times.

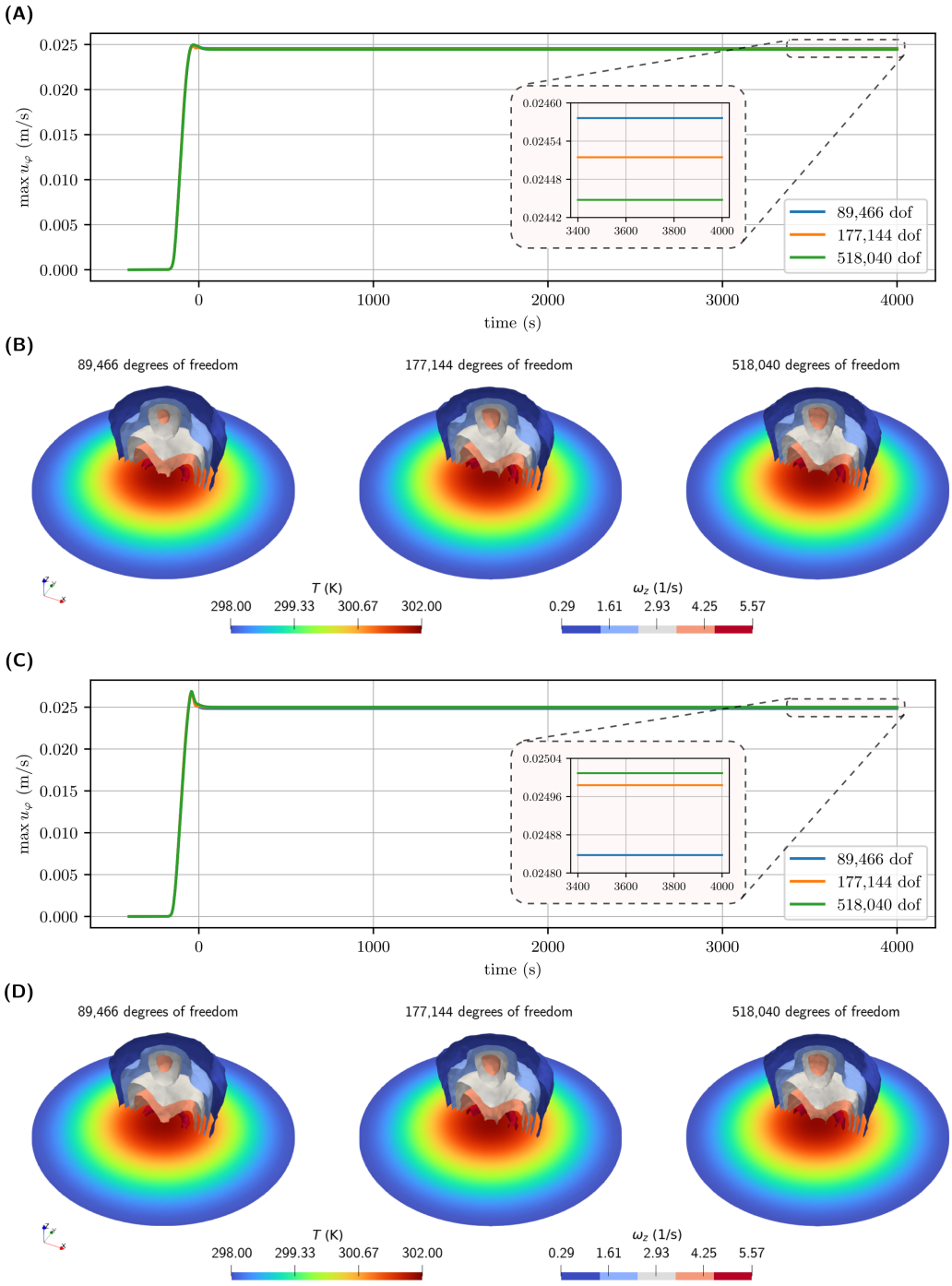

Figure 19: Mesh convergence analysis of the stationary vortex for $\beta_u = \beta_b = 5$, $\Delta T_v = 6$ K, $\delta^u = -1/3$, $\delta^b = 2/3$ and $\Omega = 0.35$ rad/s. Panels (A) and (B) correspond to the dry case ($L = 0$ J/kg), while panels (C) and (D) correspond to the moist case ($L = 2.5 \times 10^6$ J/kg). Panels (A) and (C) show the temporal evolution of the maximum azimuthal velocity, u_φ, in the domain for three computational meshes with 89 466, 177 144, and 518 040 degrees of freedom (dof). Panels (B) and (D) show clipped isosurfaces of the vertical vorticity together with a temperature slice at $z = 0.01d$ for the stationary solutions obtained on the different meshes.

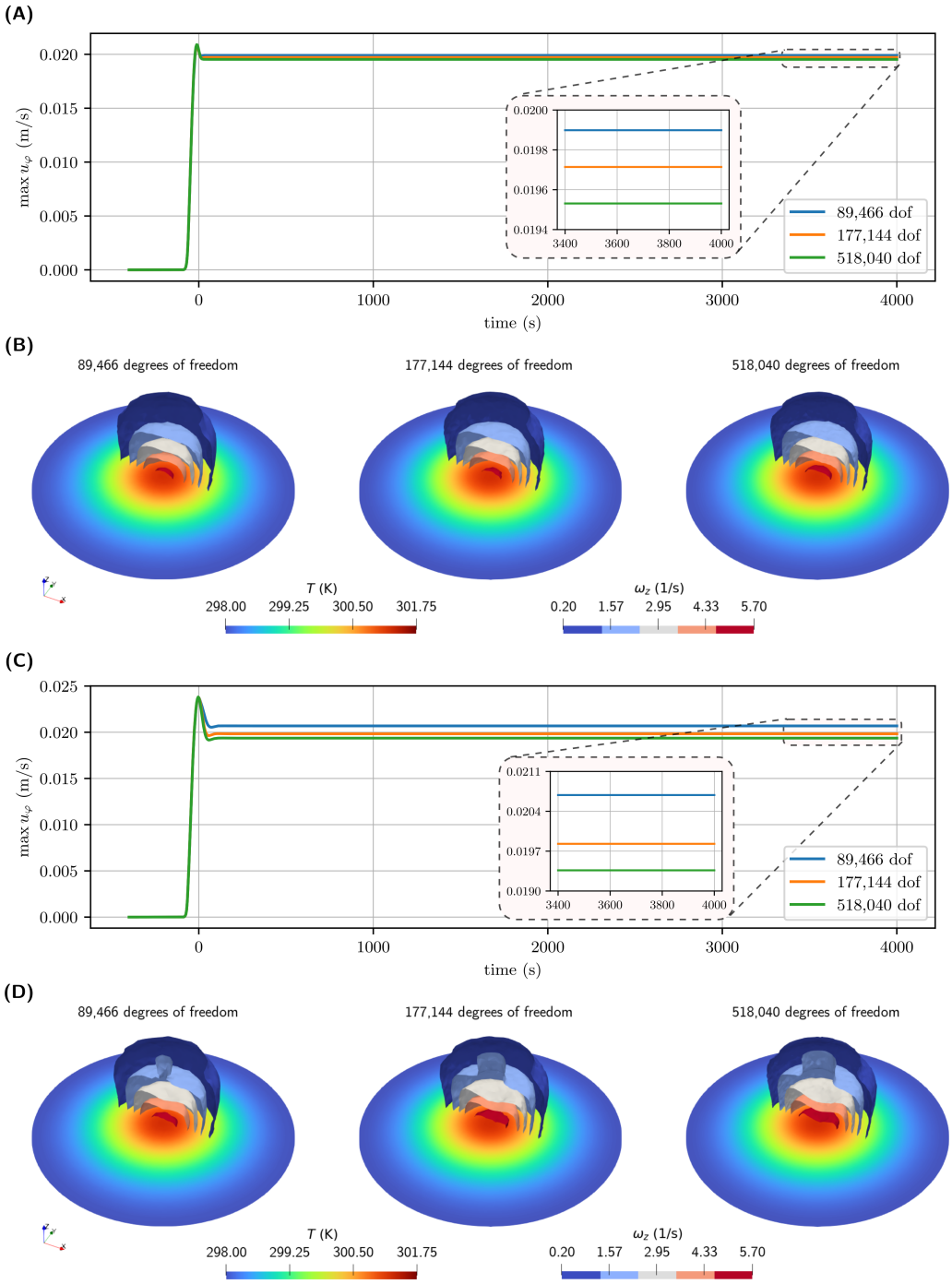

Figure 20: Mesh convergence analysis of the stationary vortex for $\beta_u = 5$, $\beta_b = 0.8$, $\Delta T_v = 5$ K, $\delta^u = -1/3$, $\delta^b = 2/3$ and $\Omega = 0.35$ rad/s. Panels (A) and (B) correspond to the dry case ($L = 0$ J/kg), while panels (C) and (D) correspond to the moist case ($L = 2.5 \times 10^6$ J/kg). Panels (A) and (C) show the temporal evolution of the maximum azimuthal velocity, u_φ, in the domain for three computational meshes with 89 466, 177 144, and 518 040 degrees of freedom (dof). Panels (B) and (D) show clipped isosurfaces of the vertical vorticity together with a temperature slice at $z = 0.01d$ for the stationary solutions obtained on the different meshes.

References

[1] Sinclair, P. C. The lower structure of dust devils. J. Atmos. Sci. **30**, 1599-1619, 1973.

[2] Balme, M. & Greeley, R. Dust devils on Earth and Mars. Rev. Geophys. **44**, RG3003, 2006.

[3] Rotunno R., The fluid dynamics of tornadoes. Annu. Rev. Fluid Mech **45** 59-84, 2013.

[4] Emanuel K. A., Divine Wind, Oxford University Press, Oxford, 2005.

[5] Davies-Jones. R. P. A review of supercell and tornado dynamics. Atmos. Res., **158-159(1)**, 274-291, 2015.

[6] Kurgansky, M. V., Lorenz, R. D., Renno, N. O., Takemi, T., Gu, Z., Wei, W. Dust devil steady-state structure from a fluid dynamics perspective. Space Sci. Rev., **203(1-4)**, 209-244, 2016.

[7] Rennó, N., Burkett, M. L., Larkin, M. P. A simple theory for dust devils. J. Atmos. Sci., **55**, 3244-3252, 1998.

[8] Rennó, N. O., Nash, A. A., Lunine, J., & Murphy, J.. Martian and terrestrial dust devils: Test of a scaling theory using Pathfinder data. Journal of Geophysical Research: Planets, **105(E1)**, 1859-1865, 2000.

[9] Castaño, D., Navarro, M. C. & Herrero H. Routes to chaos from axisymmetric vertical vortices in a rotating cylinder. Appl. Math. Model. **54**, 1-20, 2018.

[10] Castaño, D., Navarro, M. C. & Herrero, H. Cyclonic and anticyclonic rotation in a cylinder cooled inhomogeneously on the top. Chaos **31** 093108, 2021.

[11] Navarro, M. C. , Castaño, D., & Herrero H. Determining the morphology of tornado-like vortices depending on thermal gradients: a numerical study. Phys. Fluids **35**, 063605, 2023.

[12] Yanai, M., Esbensen, S., Chu, J. H. Determination of bulk properties of tropical cloud clusters from large-scale heat and moisture budgets. J. Atmos Sci. **30(4)** 611–627, 1973.

[13] Tiedtke, M. A comprehensive mass flux scheme for cumulus parameterization in large-scale models. Mon. Weather Rev. **117(8)** 1779–1800, 1989.

[14] Sobel A. H. and Bretherton C. S. Modeling tropical precipitation in a single column. J. Climate **13(24)** 4378–4392, 2000.

[15] Cheng, B., Cullen, M. J. P., Esler, J. G., Norbury, J., Turner, M. R., Vanneste, J. and Cheng, J. A model for moist convection in an ascending atmospheric column. Q. J. R. Meteorol. Soc., **143 (708)** 2925–2939, 2017.

[16] Tomassini, L. and Yang, G.-Y. Tropical moist convection as an important driver of Atlantic Hadley circulation variability. Q. J. R. Meteorol. Soc. **148 (748)** 3287-3302, 2022.

[17] Dritschel, G. N., Tobias, S. M., Parker, D. J. and Tomassini, L. Radiatively-Cooled Moist Convection under an Idealised Climate Change Scenario: Linear Analysis. arXiv preprint arXiv:2504.06019, 2025.

[18] Emanuel, K. A. Thermodynamic control of hurricane intensity. Nature, **401**, 61-100, 1999.

[19] Hernandez-Duenas, G., Majda, A. J., Smith, L. M., Stechmann, S. N. Minimal models for precipitating turbulent convection. J. Fluid Mech. **717**, 576-611, 2013.

[20] Lakkaraju, R., Stevens, R., Oresta, P., Verzicco, R., Lohse, D., Prosperetti, A. Heat transport in bubbling turbulent convection. Proc. Natl Acad. Sci. USA **110(23)**, 9237-9242, 2013.

[21] O'Gorman, P. A. Precipitation extremes under climate change. Current climate change reports. **1**, 49-59, 2015.

[22] Vallis, G. K., Parker, D. J., Tobias, S. M. A simple system for moist convection: the Rainy-Bénard model. J. Fluid Mech. **862**, 162-199, 2019.

[23] Vallis, G. K., and Penn, J. Convective organization and eastward propagating equatorial disturbances in a simple excitable system. Q. J. R. Meteorol. Soc., **146(730)**, 2297-2314, 2020.

[24] Oishi, J. S. and Brown, B. P. On the linear stability of partially and fully saturated atmospheres to moist convection. J. Fluid Mech, **1007**, A60, 2025.

[25] Agasthya, L, and Muller, C. and Cheve, M. Moist convective scaling: Insights from an idealised model. Q. J. R. Meteorol. Soc. **151**(766), e4920, 2025.

[26] Pauluis, O. and Schumacher, J. Self-aggregation of clouds in conditionally unstable moist convection. Proc. Natl. Acad. Sci. **108**(31), 12623-12628, 2011.

[27] Pauluis, O. and Schumacher, J. Radiation impacts on conditionally unstable moist convection. J. Atmos. Sci. **70**(4), 1187-1203, 2013.

[28] Chien, M.-H., Pauluis, O. M. and Almgren, A. S. Hurricane-Like Vortices in Conditionally Unstable Moist Convection. J. Adv. Model. Earth Syst. **14**(7), 1-26, 2022.

[29] Horn, S., Aurnou, J. M. Tornado-like vortices in the quasi-cyclostrophic regime of coriolis-centrifugal convection, J. Turbul. **22(4–5)**, 197–324, 2021.

[30] Rotunno R., Bryan G. H. , Nolan D. S., et al. Axisymmetric tornado simulations at high Reynolds number. J Atmos Sci. **73(10)**, 3843–3854, 2016.

[31] Lewellen W. Tornado vortex theory. Washington DC AGU Geophys. Monograph Series, **79** 19–39, 1993.

[32] Monteith, J. and Unsworth, M., Principles of Environmental Physics: Plants, Animals, and the Atmosphere. Academic Press, 2013.

[33] White, B., Gryspeerdt, E., Stier, P., Morrison, H., Thompson, G., and Kipling, Z. Uncertainty from the choice of microphysics scheme in convection-permitting models significantly exceeds aerosol effects. Atmos. Chem. Phys., **17(19)**, 12145-12175, 2017.

[34] Khain, A.P., Beheng, K.D., Heymsfield, A., Korolev, A., Krichak, S.O., Levin, Z., Pinsky, M., Phillips, V., Prabhakaran, T., Teller, A. and Van Den Heever, S.C., Representation of microphysical processes in cloud-resolving models: Spectral (bin) microphysics versus bulk parameterization. Rev. Geophys., **53(2)**, 247-322, 2015.

[35] COMSOL Multiphysics® v. 6.1. www.comsol.com. COMSOL AB, Stockholm, Sweden.

[36] Cortés, J. , Castaño, D., & Navarro, M. C. Numerical analysis of thermoconvective vortex control in a confined laminar rotating model. Phys. Fluids **38**, 043610, 2026.

[37] Aboelkassem, Y. A two-cell vortex model. Phys. Fluids **36**, 097166, 2024.